

#### Contents lists available at ScienceDirect

# Petroleum Science

journal homepage: www.keaipublishing.com/en/journals/petroleum-science



# Original Paper

# Efficient numerical modeling scheme for solving fractional viscoacoustic wave equation in TTI media and its application in reverse time migration



Lei Xiang <sup>a, b</sup>, Jian-Ping Huang <sup>a, b, \*</sup>, Qiang Mao <sup>a, b</sup>, Xin-Ru Mu <sup>a, b</sup>, Fei Li <sup>c</sup>, Juan Chen <sup>c</sup>, Jin-Tao Liu <sup>c</sup>, Min Xu <sup>c</sup>

- <sup>a</sup> Geosciences Department, China University of Petroleum (East China), Qingdao, 266580, Shandong, China
- <sup>b</sup> Pilot National Laboratory for Marine Science and Technology (Qingdao), Qingdao, 266000, Shandong, China
- <sup>c</sup> Exploration and Development Research Institute of Changqing Oilfield Branch Company Ltd., PetroChina, Xi'an, 710018, Shaanxi, China

#### ARTICLE INFO

#### Article history: Received 31 July 2024 Received in revised form 5 March 2025 Accepted 7 April 2025 Available online 10 April 2025

Edited by Meng-Jiao Zhou

Keywords: Acoustic Anisotropy Attenuation Reverse time migration

#### ABSTRACT

Amplitude dissipation and phase dispersion occur when seismic waves propagate in attenuated anisotropic media, affecting the quality of migration imaging. To compensate and correct for these effects, the fractional Laplacian pure viscoacoustic wave equation capable of producing stable and noise-free wavefields has been proposed and implemented in the Q-compensated reverse time migration (RTM). In addition, the second-order Taylor series expansion is usually adopted in the hybrid finite-difference/ pseudo-spectral (HFDPS) strategy to solve spatially variable fractional Laplacian. However, during forward modeling and Q-compensated RTM, this HFDPS strategy requires 11 and 17 fast Fourier transforms (FFTs) per time step, respectively, leading to computational inefficiency. To improve computational efficiency, we introduce two high-efficiency HFDPS numerical modeling strategies based on asymptotic approximation and algebraic methods. Through the two strategies, the number of FFTs decreased from 11 to 6 and 5 per time step during forward modeling, respectively. Numerical examples demonstrate that wavefields simulated using the new numerical modeling strategies are accurate and highly efficient. Finally, these strategies are employed for implementing high-efficiency and stable Q-compensated RTM techniques in tilted transversely isotropic media, reducing the number of FFTs from 17 to 9 and 8 per time step, respectively, significantly improving computational efficiency. Synthetic data examples illustrate the effectiveness of the proposed Q-compensated RTM scheme in compensating amplitude dissipation and correcting phase distortion.

© 2025 The Authors. Publishing services by Elsevier B.V. on behalf of KeAi Communications Co. Ltd. This is an open access article under the CC BY-NC-ND license (http://creativecommons.org/licenses/by-nc-nd/4.0/).

#### 1. Introduction

Attenuation and anisotropy are widespread properties in subsurface media, such as aligned fluid-filled fractures, low/high relief structures, and aligned minerals. These properties cause amplitude dissipation and waveform distortion as seismic waves propagate through anisotropic and attenuated media (Kjartansson, 1979; Thomsen, 1986; Carcione, 1992; Aki and Richards, 2002; Carter and Kendall, 2006; Zhu and Bai, 2019). Failure to correct and compensate for these effects during migration imaging will can lead to

reduced resolution and quality of the migrated images (Liu et al., 1976; Wang et al., 2022a; Mu et al., 2022a). To address these issues, it is crucial to develop numerical strategies that effectively compensate for both attenuation and anisotropy during migration.

Seismic viscosity is a significant characteristic in earth media, in which seismic wave propagation exhibits energy loss and phase dispersion. To describe seismic attenuation, two main models have been proposed: the standard linear solid (SLS) model (Carcione et al., 1988; Deng and McMechan, 2007) and the constant-Q (CQ) model (Kjartansson, 1979; Guo et al., 2016). The SLS attenuation

E-mail address: jphuang@upc.edu.cn (J.-P. Huang).

<sup>\*</sup> Corresponding author.

model can simulate the O effect by superposing multiple relaxation mechanisms in parallel, which has been widely used in industrial applications due to its flexibility and efficiency (Carcione, 2007; Qu et al., 2017; Mu et al., 2023). However, fitting CQ characteristics to specific frequency bands complicates the separation of dispersion and attenuation effects, which can challenge the implementation of O-compensated RTM (Liu et al., 1976; Ou et al., 2022). In contrast. the CO model has the advantage of decoupling amplitude loss and phase dispersion. Based on the CQ model, Carcione et al. (2002) introduced a time-domain temporal fractional viscoacoustic wave equation, which requires storing wavefields at each time step. Subsequent studies aimed to reduce storage demands (Zhu et al., 2014; Chen et al., 2016; Zhou et al., 2023), making Q-compensated RTM easier to apply. Recent work by Sun et al. (2024) has also expanded the O-compensated RTM methods into the frequency domain using time-fractional viscoacoustic equations based on the constant-Q model.

In recent decades, considerable research has focused on seismic wave modeling methods that consider both anisotropy and attenuation. For instance, Xie et al. (2015) developed a viscoacoustic wave equation in transversely isotropic (TI) media based on Duveneck and Bakker's (2011) anisotropic acoustic wave equation. Xu et al. (2015) proposed a pure viscoacoustic wave equation incorporating the single-SLS model. Fathalian et al. (2021) extended this by developing a viscoacoustic TTI wave equation, accounting for amplitude attenuation and phase dispersion in TTI media. However, these models typically assume velocity anisotropy and attenuation isotropy. Petrophysical experiments, however. show that attenuation anisotropy, along with velocity anisotropy, is common in subsurface media (Tao and King, 1990; Lynn et al., 1999; Zhubayev et al., 2016). To capture these effects, Da Silva et al. (2019) proposed a viscoacoustic TTI wave equation to describe anisotropic attenuation in attenuating TTI media, while Zhang et al. (2020) introduced pseudo-viscoacoustic VTI wave equations. Unfortunately, these pseudo-viscoacoustic TI wave equations become unstable when the anisotropic parameter  $\varepsilon < \delta$ , leading to shear-wave artifacts (Mao et al., 2024a). To overcome these issues, the fractional Laplacian pure viscoacoustic wave equation has been proposed, based on the CQ model, and applied in Q-compensated RTM (Zhang et al., 2022; Mu et al., 2022b; Xiang et al., 2025). However, in heterogeneous media, the mixed-domain fractional Laplacian operator varies with the quality factor, which complicates its direct solution (Yao et al., 2017; Xing and Zhu, 2019). The traditional approach for solving this issue is the second-order Taylor series expansion in the HFDPS strategy, which requires calculating 11 FFTs per time step during forward modeling. This high computational demand limits the practical application of traditional HFDPS strategies in real production environments.

Attenuation compensation is critical for high-quality imaging in attenuated media. However, during wavefield extrapolation, high-frequency noise can be amplified during compensation, leading to instability in the resulting images (Zhu et al., 2014; Li and Qu, 2022; Wang et al., 2022b; Mu et al., 2023). To stabilize attenuation-compensated RTM, low-pass filters are commonly used in the wavenumber domain to suppress high-frequency noise. However, their application can inadvertently suppress some useful signal, particularly when the velocity and Q models vary significantly

(Yang et al., 2021; Mu et al., 2023). Additionally, when seismic data contains substantial random noise, low-pass filtering can unintentionally remove relevant signal components. To address these challenges, the stabilization factor method has been proposed, which automatically suppresses high-frequency noise and operates in the time-space domain, preserving more of the signal's integrity (Wang et al., 2022a; Chen et al., 2020; Mao et al., 2024b). However, the stabilization factor method increases the number of FFTs per time step from 11 to 17, posing computational challenges for large-scale simulations.

In this study, we propose two high-efficiency numerical strategies to address the computational cost and instability challenges in Q-compensated RTM for attenuating anisotropic media. First, we introduce an algebraic method for the HFDPS strategy, reducing the number of Fourier transforms per time step and significantly improving computational efficiency. Building on this strategy, we derive a stable and efficient anisotropic attenuation-compensated extrapolation operator and successfully implement Q-compensated RTM in attenuating TTI media. Through synthetic examples, we demonstrate that the new Q-compensated TTI RTM method effectively compensates for waveform distortion and amplitude attenuation due to anisotropy, achieving high computational efficiency. We also explore an enhancement to the HFDPS strategy using an asymptotic approximation method, further improving computational efficiency in Q-compensated RTM. These strategies provide effective tools for Q-compensated RTM in attenuating anisotropic media, improving both computational efficiency and imaging quality in real seismic data.

#### 2. Theory

#### 2.1. Review of the traditional HFDPS numerical solution strategy

To accurately describe the attenuation effect in anisotropic media, based on Kjartansson's CQ attenuation model, Xiang et al. (2025) proposed the approximated complex-valued dispersion relation in attenuation VTI media:

$$\omega^{2} \approx M_{11}k_{x}^{2} + M_{33}k_{z}^{2} + \frac{\left(M_{13}^{2}\left(\sqrt{M_{11}M_{33}}\right)^{-1} - \sqrt{M_{11}M_{33}}\right)k_{x}^{2}k_{z}^{2}}{k_{x}^{2} + k_{z}^{2}},$$
(1)

where  $\omega$  is the angular frequency.  $k_x$  and  $k_z$  denote spatial wavenumbers along the horizontal and vertical directions, respectively.  $M_{ij}(\omega) = C_{ij} \cos^2(\pi \gamma_{ij}/2) \left(\frac{i\omega}{\omega_0}\right)^{2\gamma_{ij}}$  represent the complex stiffness components.  $\gamma_{ij} = \arctan(1/Q_{ij})/\pi$  are dimensionless parameters,  $0 < \gamma_{ij} < 1/2$ , and for any positive value of  $Q_{ij}$ .  $C_{ij}$  and  $Q_{ij}$  are the elastic stiffness constants and the quality factor, respectively. In addition,  $C_{33} = \rho v_P^2$ ,  $C_{11} = C_{33}(1+2\varepsilon)$ , and  $C_{13} = C_{33}\sqrt{(1+2\delta)}$ .  $\varepsilon$  and  $\delta$  are Thomsen anisotropic parameters (Thomsen, 1986).  $Q_{13} = 2Q_{33}/(\delta_Q C_{33}^2/C_{13}^2 + 2)$ ,  $Q_{11} = Q_{33}/(1+\varepsilon_Q)$ , and  $Q_{33} = Q_p$ .  $\varepsilon_Q$  and  $\delta_Q$  denote Thomsen-type attenuation anisotropy parameters (Zhu and Tsvankin, 2006). To improve readability and facilitate understanding, we define the following conventions:

$$\Psi_{11} = \cos^2 \phi \frac{\partial^2}{\partial x^2} - \sin 2\phi \frac{\partial^2}{\partial x \partial z} + \sin^2 \phi \frac{\partial^2}{\partial z^2}, \Psi_{33} = \sin^2 \phi \frac{\partial^2}{\partial x^2} + \sin 2\phi \frac{\partial^2}{\partial x \partial z} + \cos^2 \phi \frac{\partial^2}{\partial z^2},$$

$$\widehat{\Psi}_{11} = \cos^2 \phi \frac{\partial^4}{\partial x^4} + \sin^2 \phi \frac{\partial^4}{\partial z^4} + \frac{\partial^4}{\partial x^2 \partial z^2} - \sin 2\phi \left( \frac{\partial^4}{\partial x^3 \partial z} + \frac{\partial^4}{\partial x \partial z^3} \right),$$

$$\widehat{\Psi}_{33} = \sin^2 \phi \frac{\partial^4}{\partial x^4} + \cos^2 \phi \frac{\partial^4}{\partial z^4} + \frac{\partial^4}{\partial x^2 \partial z^2} + \sin 2\phi \left( \frac{\partial^4}{\partial x^3 \partial z} + \frac{\partial^4}{\partial x \partial z^3} \right),$$

$$\Psi_{13} = \begin{pmatrix} \sin^2 \phi \cos^2 \phi \left( \frac{\partial^4}{\partial x^4} + \frac{\partial^4}{\partial z^4} \right) + \left( \cos^4 \phi + \sin^4 \phi - \sin^2 2\phi \right) \frac{\partial^4}{\partial x^2 \partial z^2} \\ + \sin 2\phi \left( \cos^2 \phi - \sin^2 \phi \right) \frac{\partial^4}{\partial x^3 \partial z} + \sin 2\phi \left( \sin^2 \phi - \cos^2 \phi \right) \frac{\partial^4}{\partial x \partial z^3} \right),$$

$$(2)$$

where  $\phi$  is the tilt angle. In addition, we also define the following conventions:

$$L_{1} = \mathcal{F}^{-1}(\mathcal{F}(p)\ln(k)), L_{2} = \mathcal{F}^{-1}\left(\mathcal{F}(p)\ln(k)^{2}\right), L_{3} = \mathcal{F}^{-1}\left(k^{-1}\mathcal{F}\left(\frac{\partial p}{\partial t}\right)\right),$$

$$L_{4} = \mathcal{F}^{-1}\left(k^{-1}\mathcal{F}\left(\frac{\partial p}{\partial t}\right)\ln(k)\right), L_{5} = \mathcal{F}^{-1}\left(k^{-1}\mathcal{F}\left(\frac{\partial p}{\partial t}\right)\ln(k)^{2}\right),$$

$$L_{6} = \mathcal{F}^{-1}\left(\left(k_{x}^{2} + k_{z}^{2}\right)^{-1}\mathcal{F}(p)\right), L_{7} = \mathcal{F}^{-1}\left(\left(k_{x}^{2} + k_{z}^{2}\right)^{-1}\mathcal{F}(p)\ln(k)\right),$$

$$L_{8} = \mathcal{F}^{-1}\left(\left(k_{x}^{2} + k_{z}^{2}\right)^{-1}\mathcal{F}(p)\ln(k)^{2}\right), L_{9} = \mathcal{F}^{-1}\left(k^{-1}\left(k_{x}^{2} + k_{z}^{2}\right)^{-1}\mathcal{F}\left(\frac{\partial p}{\partial t}\right)\right),$$

$$L_{10} = \mathcal{F}^{-1}\left(k^{-1}\left(k_{x}^{2} + k_{z}^{2}\right)^{-1}\mathcal{F}\left(\frac{\partial p}{\partial t}\right)\ln(k)\right), L_{11} = \mathcal{F}^{-1}\left(k^{-1}\left(k_{x}^{2} + k_{z}^{2}\right)^{-1}\mathcal{F}\left(\frac{\partial p}{\partial t}\right)\ln(k)^{2}\right),$$

where  $\mathscr{T}$  and  $\mathscr{T}^{-1}$  represent forward Fourier transform and inverse Fourier transform, respectively. Subsequently, based on the work of Xiang et al. (2025), the traditional HFDPS strategy is used to discrete the pure viscoacoustic TTI wave equation, which can be written as

where f is the source-time function, and  $\zeta_{ij}$ ,  $\chi_{ij}$ ,  $a_i$ ,  $b_i$  can be expressed as

$$\begin{split} \frac{\partial^{2}p}{\partial t^{2}} &= \Psi_{11} \Big( \zeta_{11} \Big( p + 2\gamma_{11}(x)L_{1} + 2\gamma_{11}^{2}(x)L_{2} \Big) + \chi_{11} \Big( L_{3} + 2L_{4}\gamma_{11}(x) + 2\gamma_{11}^{2}(x)L_{5} \Big) \Big) \\ &+ \Psi_{33} \Big( \zeta_{33} \Big( p + 2\gamma_{33}(x)L_{1} + 2\gamma_{33}^{2}(x)L_{2} \Big) + \chi_{33} \Big( L_{3} + 2L_{4}\gamma_{33}(x) + 2\gamma_{33}^{2}(x)L_{5} \Big) \Big) \\ &- \Psi_{13} \begin{pmatrix} a_{1} \Big( L_{6} + 2L_{7}\lambda_{33}\gamma_{33}(x) + 2(\lambda_{33}\gamma_{33}(x))^{2}L_{8} \Big) \\ &+ b_{1} \Big( L_{9} + 2L_{10}\lambda_{33}\gamma_{33}(x) + 2L_{11}(\lambda_{33}\gamma_{33}(x))^{2} \Big) \\ &- a_{2} \Big( L_{6} + 2L_{7}\lambda_{11}\gamma_{11}(x) + 2(\lambda_{11}\gamma_{11}(x))^{2}L_{8} \Big) \\ &- b_{2} \Big( L_{9} + 2L_{10}\lambda_{11}\gamma_{11}(x) + 2L_{11}(\lambda_{11}\gamma_{11}(x))^{2} \Big) \end{pmatrix} \end{split}$$

$$\begin{split} \zeta_{ij} &= C_{ij}^{\left(\gamma_{ij}+1\right)} \cos^2\left(\pi\gamma_{ij}\middle/2\right) \omega_0^{-2\gamma_{ij}} \cos\left(\pi\gamma_{ij}\right), \\ \chi_{ij} &= C_{ij}^{\left(\gamma_{ij}+1/2\right)} \cos^2\left(\pi\gamma_{ij}\middle/2\right) \omega_0^{-2\gamma_{ij}} \sin\left(\pi\gamma_{ij}\right), \\ a_1 &= (\zeta_{13})^2 \left(\sqrt{\zeta_{11}\zeta_{33}}\right)^{-1}, \\ b_1 &= (\chi_{13})^2 \left(\sqrt{\chi_{11}\chi_{33}}\right)^{-1}, \\ a_2 &= \sqrt{\zeta_{11}\zeta_{33}}, \\ b_2 &= \sqrt{\chi_{11}\chi_{33}}. \end{split}$$

In addition, to facilitate the subsequent discussion, we have referred to these 2-order partial derivatives terms (i.e.  $\frac{\partial^2}{\partial x^2}$ ,  $\frac{\partial^2}{\partial x\partial z}$ ,  $\frac{\partial^2}{\partial x^2}$ ) as the elliptic term and the 4-order partial derivatives terms (e.g.  $\frac{\partial^4}{\partial x^4}$ ,  $\frac{\partial^4}{\partial x^2\partial z^2}$ ,  $\frac{\partial^4}{\partial x^2\partial z^2}$ ) as the correction term.

By comparing  $L_1-L_5$  with  $L_7-L_{11}$  terms in Eq. (3), we can see that these  $L_7-L_{11}$  terms have only the common term  $(k_\chi^2+k_\chi^2)^{-1}$  more than these  $L_1-L_5$  terms. If we could eliminate the fractional form  $(k_\chi^2+k_\chi^2)^{-1}$  of these  $L_7-L_{11}$  terms or construct a fractional form  $(k_\chi^2+k_\chi^2)^{-1}$  in these  $L_1-L_5$  terms, we reduce the number of FFTs from 11 to 6 or 5 per time step. By analyzing Eq. (1) and Eq. (4), we can find that since the elliptic term in Eq. (1) does not contain the fractional term  $\frac{1}{k_\chi^2+k_z^2}$ , it is inconsistent with the form of the correction term, resulting in additional 6 FFTs calculations per time step in forward modeling. Therefore, we can eliminate the fractional form  $\frac{1}{k_\chi^2+k_z^2}$  of the correction term or construct a fractional form  $\frac{1}{k_\chi^2+k_z^2}$  in the elliptic term of Eq. (1), which reduces the number of FFTs from 11 to 6 or 5 per time step, improving the computational

# 2.2. High-efficiency HFDPS numerical solution strategy

To reduce the calculation numbers of FFTs, we propose a new high-efficiency HFDPS (HE-HFDPS) numerical modeling strategy based on algebraic methods. We introduce the expression  $\frac{k_2^2+k_2^2}{k_x^2+k_2^2}$  into the elliptic term of Eq. (1) to construct the fractional form  $\frac{1}{k_x^2+k_2^2}$ , which can unify the denominator form of the elliptic term and the correction term of Eq. (1). In addition, this method without approximations requires only algebraic operations, then Eq. (1) can be rewritten as

$$\omega^{2} \approx \frac{\left(M_{11}k_{x}^{2} + M_{33}k_{z}^{2}\right)\left(k_{x}^{2} + k_{z}^{2}\right)}{k_{x}^{2} + k_{z}^{2}} + \frac{\left(M_{13}^{2}\left(\sqrt{M_{11}M_{33}}\right)^{-1} - \sqrt{M_{11}M_{33}}\right)k_{x}^{2}k_{z}^{2}}{k_{x}^{2} + k_{z}^{2}}.$$
 (5)

Subsequently, similarly to the derivation from our previous work in Xiang et al. (2025), a new efficient pure viscoacoustic TTI wave equation can be obtained:

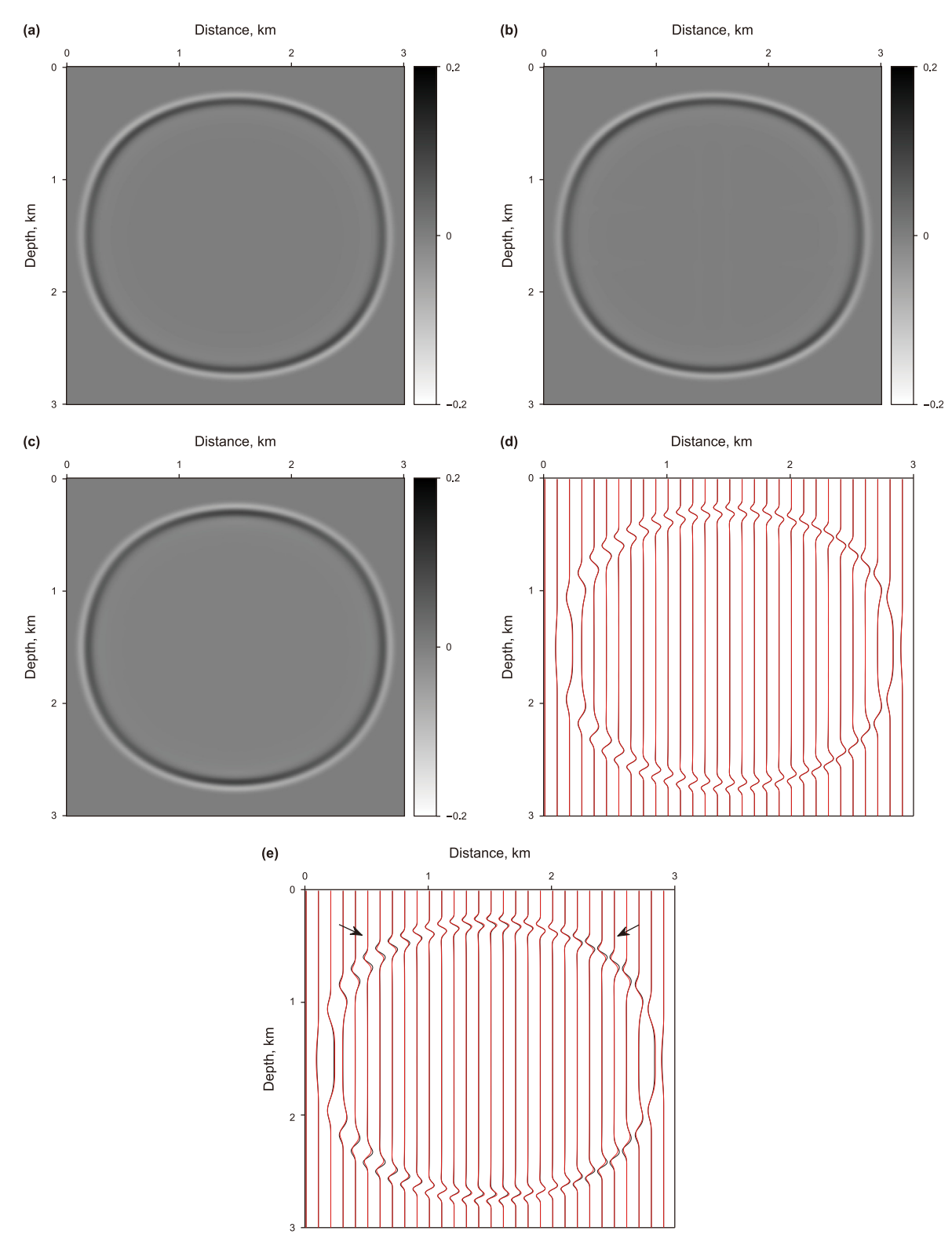
$$\frac{\partial^{2} p}{\partial t^{2}} = \frac{1}{\frac{\partial^{2}}{\partial x^{2}} + \frac{\partial^{2}}{\partial z^{2}}} \begin{pmatrix}
\widehat{\Psi}_{11} \begin{pmatrix} \zeta_{11} \left( -\nabla^{2} \right)^{\gamma_{11}} \\
+ \chi_{11} \frac{\partial}{\partial t} \left( -\nabla^{2} \right)^{\gamma_{11}-1/2} \end{pmatrix} + \widehat{\Psi}_{33} \begin{pmatrix} \zeta_{33} \left( -\nabla^{2} \right)^{\gamma_{33}} \\
+ \chi_{33} \frac{\partial}{\partial t} \left( -\nabla^{2} \right)^{\gamma_{33}-1/2} \end{pmatrix} \\
+ \Psi_{13} \begin{pmatrix} a_{1} \left( -\nabla^{2} \right)^{\mu_{33}\gamma_{33}} + b_{1} \frac{\partial}{\partial t} \left( -\nabla^{2} \right)^{\mu_{33}\gamma_{33}-1/2} \\
- a_{2} \left( -\nabla^{2} \right)^{\mu_{11}\gamma_{11}} - b_{2} \frac{\partial}{\partial t} \left( -\nabla^{2} \right)^{\mu_{11}\gamma_{11}-1/2} \end{pmatrix}$$

$$P + f.$$
(6)

efficiency.

Similar to the derivation of Eq. (4), using the HE-HFDPS strategy to simulate the pure viscoacoustic TTI wave equation as follows:

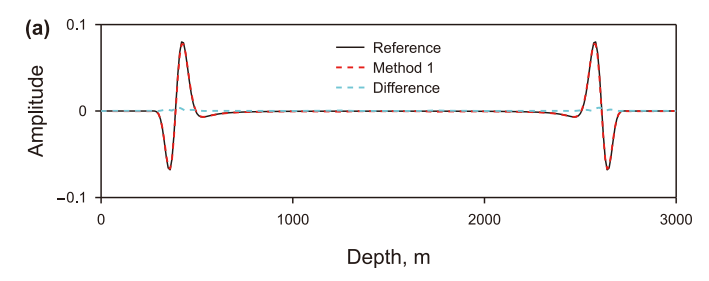
$$\frac{\partial^{2} p}{\partial t^{2}} = -\widehat{\Psi}_{11} \Big( \zeta_{11} \Big( L_{6} + 2\gamma_{11}(x)L_{7} + 2\gamma_{11}^{2}(x)L_{8} \Big) + \chi_{11} \Big( L_{9} + 2\gamma_{11}(x)L_{10} + 2\gamma_{11}^{2}(x)L_{11} \Big) \Big) 
- \widehat{\Psi}_{33} \Big( \zeta_{33} \Big( L_{6} + 2\gamma_{33}(x)L_{7} + 2\gamma_{33}^{2}(x)L_{8} \Big) + \chi_{33} \Big( L_{9} + 2\gamma_{33}(x)L_{10} + 2\gamma_{33}^{2}(x)L_{11} \Big) \Big) 
- \Psi_{13} \begin{pmatrix} a_{1} \Big( L_{6} + 2L_{7}\lambda_{33}\gamma_{33}(x) + 2(\lambda_{33}\gamma_{33}(x))^{2}L_{8} \Big) \\ + b_{1} \Big( L_{9} + 2L_{10}\lambda_{33}\gamma_{33}(x) + 2L_{11}(\lambda_{33}\gamma_{33}(x))^{2} \Big) \\ - a_{2} \Big( L_{6} + 2L_{7}\lambda_{11}\gamma_{11}(x) + 2(\lambda_{11}\gamma_{11}(x))^{2}L_{8} \Big) \\ - b_{2} \Big( L_{9} + 2L_{10}\lambda_{11}\gamma_{11}(x) + 2L_{11}(\lambda_{11}\gamma_{11}(x))^{2} \Big) \Big) + f.$$
(7)



**Fig. 1.** Wavefield snapshots at 0.4 s by simulating (a) the reference HFDPS strategy Eq. (4), (b) the proposed HE-HFDPS strategy Eq. (7) based on the algebraic method, and (c) the proposed HE-HFDPS strategy Eq. (C.9) based on the asymptotic approximation method. Note that (d) and (e) are comparisons of the wavefield snapshots of (a) with (b) and (c) in wiggle format, respectively.

From the above Eq. (7), we will find that Eq. (7) only retains  $(L_6-L_{11})$  compared to the traditional strategy Eq. (4)  $(L_1-L_{11})$ , reducing the number of FFTs from 11 to 6 per time step. It shows that the proposed HE-HFDPS numerical modeling strategy has significant potential for improved computational efficiency in

forward modeling. In addition, Eq. (5) does not adopt extra approximation compared with the original approximated complex-valued dispersion relation (Eq. (1)). Therefore, the wavefield simulation accuracy of this scheme is equivalent to that of the original HFDPS numerical modeling strategy. In the subsequent realization



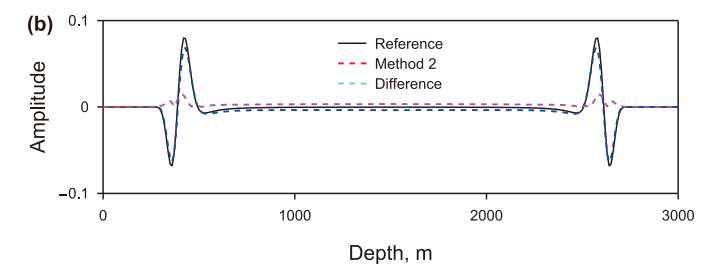


Fig. 2. Trace comparison at a horizontal distance of 0.9 km. (a) The black solid line and the red dashed line denote the trace from Fig. 1(a) and (b), respectively. The blue dashed line is the difference between the black solid and red dashed lines. (b) The black solid line and the blue dashed line denote the trace from Fig. 1(a) and (c), respectively. The pink dashed line is the difference between the black solid and blue dashed lines. Method 1 and Method 2 represent the algebraic and asymptotic approximation methods, respectively.

of attenuation compensation RTM, Eq. (7) is used as the attenuation source formula to derive the efficient and stable Q-compensated wavefield modeling operator.

#### 2.3. Analysis of the proposed HE-HFDPS strategies

To facilitate the analysis of the accuracy, robustness, and computational efficiency of different strategies, we compare the traditional HFDPS strategy Eq. (4), the HE-HFDPS strategy based on the algebraic method Eq. (7), and the HE-HFDPS strategy based on the asymptotic approximation method Eq. (D.9) together. Note that the HE-HFDPS strategy based on the asymptotic approximation method is discussed in the Discussion section. All experiments are implemented using the MATLAB 2021a platform on the same computer with an Intel(R) Core (TM) i3-6100 CPU@3.70GHz, memory of 16G.

#### 2.3.1. Accuracy analysis

To evaluate the stability of the proposed HE-HFDPS strategy when  $\varepsilon < \delta$  and its accuracy in anisotropic attenuation media. We designed a homogeneous VTI model with a size of 301  $\times$  301 for the numerical experiments, and the size of the vertical and horizontal grids is 10 m. A Ricker wavelet is located at (1510 m, 1510 m) as the source, and the peak frequency is 25 Hz. The time step for the numerical simulation is 1 ms. The model parameters are as follows:  $\varepsilon = 0.1$ ,  $\delta = 0.25$ ,  $\varepsilon_Q = 0.4$ ,  $\delta_Q = -0.1$ ,  $\nu_P = 3000$  m/s, and Q = 30

Fig. 1 shows the wavefield snapshots of different strategies at 0.4 s, calculated by the traditional HFDPS strategy (Fig. 1(a)), the proposed HE-HFDPS strategy based on the algebraic method (Method 1) (Fig. 1(b)), and the asymptotic approximation method (Method 2) (Fig. 1(c)), respectively. In Fig. 1, when the anisotropy parameter  $\varepsilon < \delta$ , the proposed two highly efficient numerical simulation methods can obtain stable wavefield snapshots. To compare the simulated accuracy, Fig. 1(d) and (e) present the wavefield snapshots of Fig. 1(b) and (c) overlaying Fig. 1(a), respectively. From Fig. 1(d), the wavefield generated by the proposed HE-HFDPS strategy based on Method 1 aligns perfectly with the reference trace. However, the HE-HFDPS strategy based on Method 2 deviates significantly from the reference (shown by the black arrow).

For a more detailed comparison, Fig. 2 displays the vertical traces at the horizontal distances of 0.9 km extracted from Fig. 1. In Fig. 2(a), the numerical result obtained from the HE-HFDPS strategy based on Method 1 (the dashed red line) aligns with the result obtained from the reference HFDPS strategy (the solid black line). In addition, the blue dotted line represents the absolute difference between the track of Method 1 and the reference track, which is close to zero. From Fig. 2(b), the HE-HFDPS strategy based on Method 2 significantly deviates from the reference line. These results are consistent with the theoretical analysis provided in the previous section, that the algebraic method has the wavefield simulation accuracy equivalent to the original HFDPS numerical

modeling strategy. However, the numerical simulation strategy based on the asymptotic approximation method will lead to the imbalance of the propagation amplitude, but fortunately, the phase information is relatively accurate. The asymptotic approximation method will be discussed in more detail in the Discussion section.

#### 2.3.2. Robustness analysis

To verify the robustness of the HE-HFDPS strategies based on the algebraic method and the asymptotic approximation method in complex media, the BP TTI model was used to simulate the wavefield. Fig. 3 shows the complex BP TTI model, which is discretized into a grid of  $787 \times 451$ . The vertical and horizontal grid spacing is 10 m. The Ricker wavelet with a dominant frequency of 20 Hz is placed on the surface at 3985 m. The time step for the numerical simulation is 0.8 ms, and the reference frequency is 20 Hz.

Fig. 4 displays wavefield snapshots simulated by the Zhang et al. (2020b) proposed coupled pseudo-viscoacoustic TTI wave equation (Fig. 4(a)—(b)), the proposed HE-HFDPS strategies based on the algebraic method (Fig. 4(c)—(d)), and the asymptotic approximation method (Fig. 4(e)—(f)) at t=1.6 s and t=2.4 s, respectively. Fig. 4(a) and (b) show wavefield snapshots are numerical instabilities. However, the wavefield snapshots in Fig. 4(c)—(d) and 4(e)—(f) simulated by the proposed two HE-HFDPS strategies are stable. These findings illustrate that the HE-HFDPS strategies based on the algebraic method and the asymptotic approximation method can obtain stable simulated wavefields in complex attenuation media.

#### 2.3.3. Efficiency analysis

To analyze the computational efficiency, we list the number of forward and inverse Fourier transforms required for each time step of the traditional HFDPS and HE-HFDPS strategies in forward modeling and Q-compensated RTM in Tables 1 and 2, respectively. Table 1 indicates that the proposed HE-HFDPS strategy can reduce the number of FFTs from 11 to 6 and 5 in forward modeling, respectively. Similarly, Table 2 shows a reduction in FFTs from 17 to 9 and 8 for O-compensated RTM, respectively. Then, to further validate the computational efficiency of the proposed numerical solution strategies in forward modeling, these homogeneous media with sizes of 101  $\times$  101, 301  $\times$  301, and 601  $\times$  601 are conducted forward simulation of different numerical modeling strategies. The recording time is 0.8 s, and the model parameters are  $\nu_{p}=$ 2500 m/s,  $\varepsilon_{\rm Q}=$  0.4,  $\delta_{\rm Q}=-$  0.1,  $\varepsilon=$  0.35,  $\delta=$  0.1,  $\rm Q=20$  and  $\phi=$ 45°. The sponge absorption boundary has a thickness of 50 grid points.

In addition, to show the improvement of computational efficiency more clearly, we construct the efficiency improvement ratio (EIR) formula as follows:

EIR = 
$$\left(\frac{1}{t_{M_i}} - \frac{1}{t_R}\right) / \frac{1}{t_R} \times 100\%, \quad i = 1, 2$$
 (8)

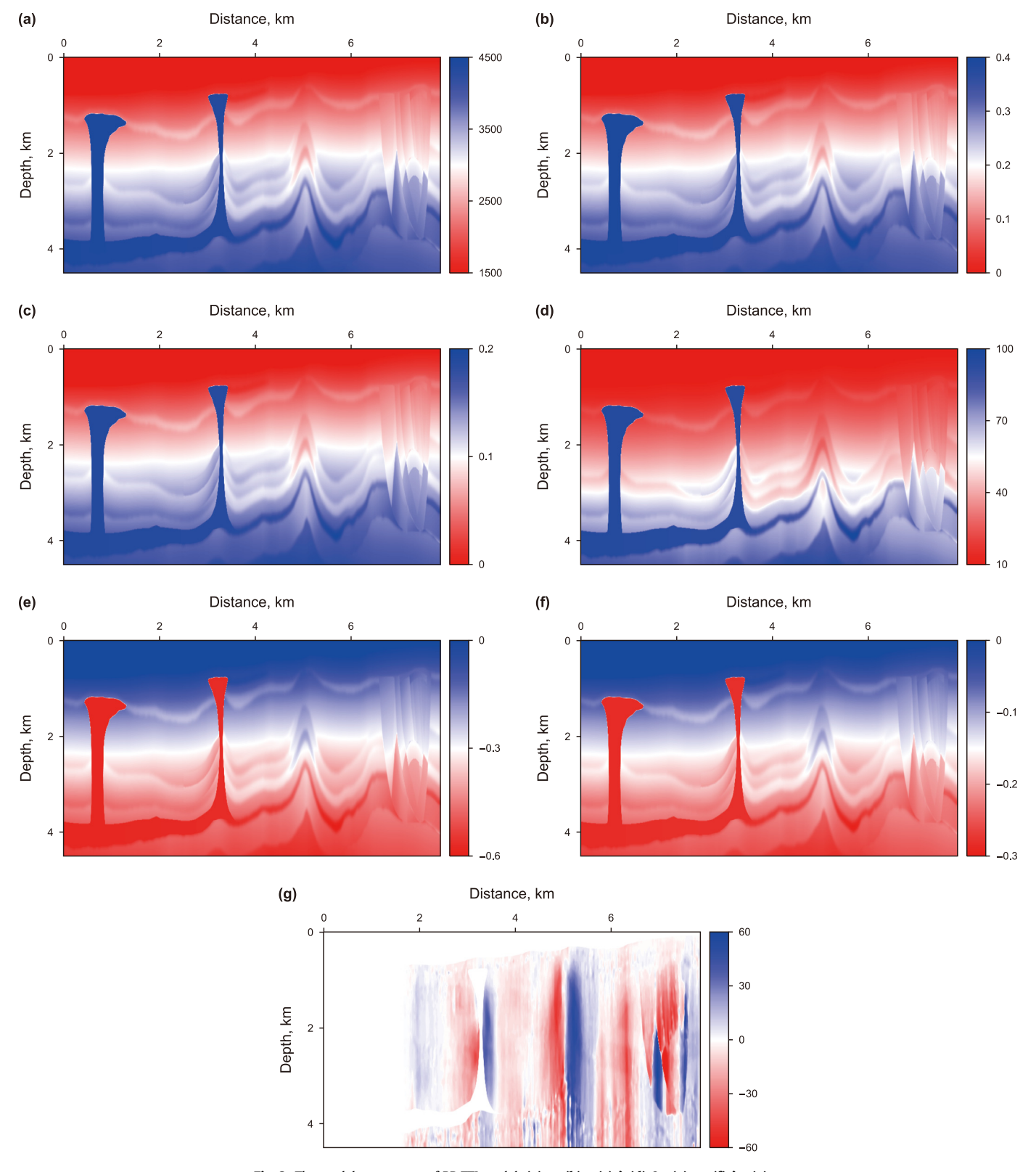


**Fig. 3.** The model parameters of BP TTI model: (a)  $v_p$ , (b)  $\varepsilon$ , (c)  $\delta$ , (d)  $Q_p$ , (e)  $\varepsilon_Q$ , (f)  $\delta_Q$ , (g)  $\phi$ .

where  $t_{\rm R}$  is the reference strategy running time,  $t_{\rm M_i}$  represents the simulation running time of the algebraic method or the asymptotic approximation method.

Tables 3 and 4 show the running time and efficiency improvement ratio of using algebraic and asymptotic approximation

methods to simulate 0.8 s wavefield snapshots, respectively. The running time comparison in Tables 3 and 4 demonstrates that the numerical solution times for the proposed HE-HFDPS strategies are shorter than that of the reference HFDPS strategy. In particular, the computational efficiency of the newly proposed numerical

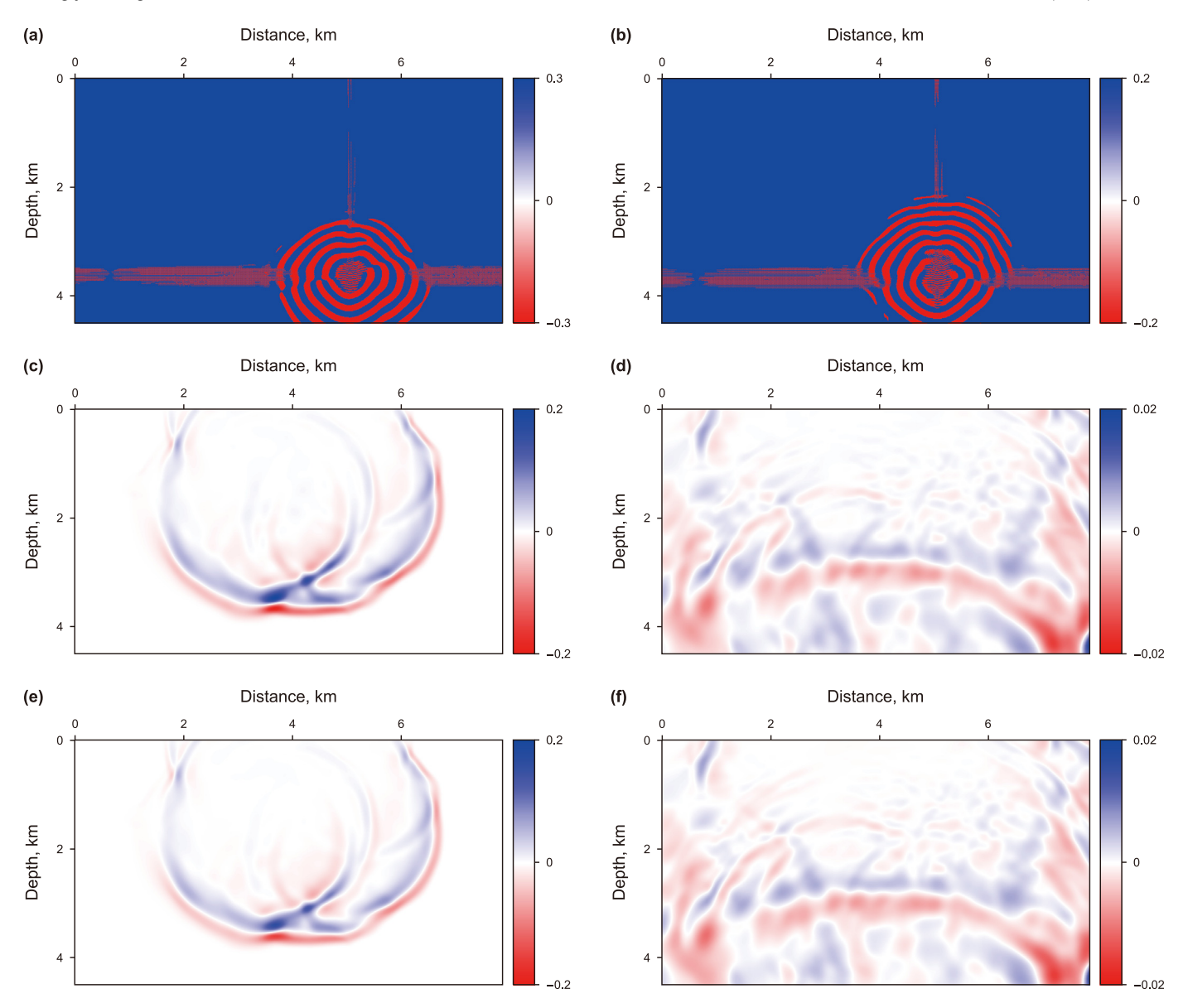


**Fig. 4.** Wavefield snapshots at t = 1.6 s, and t = 2.4 s simulated by the pseudo-viscoacoustic TTI wave equation ((a), (b)), the newly proposed HE-HFDPS strategy based on the algebraic method ((c), (d)), and the HE-HFDPS based on the asymptotic approximation method ((e), (f)), respectively.

**Table 1**The number of forward Fourier transforms (FTs) and inverse Fourier transforms required at each time step for the numerical solution of the forward modeling using different numerical simulation strategies.

	Method			
	Reference	Algebraic time	Asymptotic approximation time	
Forward FTs	2	2	2	
Inverse FTs	11	6	5	

**Table 2**The number of forward Fourier transforms and inverse Fourier transforms required at each time step for the numerical solution of the Q-compensated RTM using different numerical simulation strategies.

	Method				
	Reference	Algebraic time	Asymptotic approximation time		
Forward FTs	2	2	2		
Inverse FTs	17	9	8		

**Table 3**The running time and efficiency improvement ratio (EIR) of using the reference and algebraic methods to simulate 0.8 s wavefield snapshots in forward modeling.

Model size	Method				
	Reference time, s	Algebraic time, s	EIR		
101 × 101 301 × 301 601 × 601	201.57 961.28 3559.05	121.29 573.08 2056.58	66.53% 67.73% 73.06%		

modeling strategies can be nearly doubled compared with the reference strategy, and the asymptotic approximation method has a higher computational efficiency than the algebraic method. That is because, for each time step of the forward modeling, the asymptotic approximation method only needs to solve 5 FFTs, while the algebraic method solves 6 FFTs. In addition, the asymptotic approximation method does not contain any fourth-order partial derivatives, only second-order partial derivatives.

**Table 4**The running time and efficiency improvement ratio (EIR) of using the reference and asymptotic approximation methods to simulate 0.8 s wavefield snapshots in forward modeling.

Model size	Method				
	Reference time, s	Algebraic time, s	EIR		
101 × 101	201.57	93.28	116.09%		
$301 \times 301$	961.28	409.93	134.50%		
$601 \times 601$	3559.05	1430.91	148.72%		

# 2.4. Derivation and implementation of efficient and stable Q-compensated RTM

To implement anisotropic attenuation-compensated RTM, by reversing the sign of the amplitude attenuation term ( $\chi_{ij}$  terms and  $b_{ij}$  terms) and maintaining the phase dispersion term ( $\zeta_{ij}$  terms and  $a_{ij}$  terms) unchanged in Eq. (6), we can achieve attenuation-compensated wavefield extrapolation. Then, the anisotropic attenuation-compensated extrapolation operator can be written as

$$P(t + \Delta t, \omega) = P(t, \omega) \exp\left[-i\Delta t \omega_0^{\gamma} \omega^{1-\gamma}\right] \times \exp\left[\Delta t \omega_0^{\gamma} \omega^{1-\gamma} \tan(\pi \gamma / 2)\right], \tag{10}$$

where  $\Delta t$  denote the time interval of seismic wave propagation. In Eq. (10), the real part represents the amplitude compensation term, which increases exponentially with frequency. To avoid the instability of attenuation-compensation numerical simulation in isotropic attenuation media, Mu et al. (2023) proposed a stable term  $\Upsilon(1-\tau\omega)\omega$  into the real part of Eq. (10), where  $\tau=1/(2\omega_{\tau})$  is the stability factor and  $\Upsilon$  is a constant that is associated with  $\tau$ . In addition, the parameter  $\omega_{\tau} \approx 2\pi (f_{\tau} + f_{s})$ , where  $f_{s}$  denote the dominant frequency of the source wavelet.  $f_{\tau}$  denotes the increment of frequency. Through numerous numerical experiments, Mu et al. (2023) concluded that the  $f_{\tau} \in (5, 20)$ . The detailed steps of how to accurately obtain the stabilization parameter  $\tau$  have been given in the work of Mu et al. (2023). In particular, the effectiveness of this method for suppressing high-frequency noise in attenuating anisotropic media has been demonstrated in the work of Mao et al. (2024a). Thus, we do not discuss them in detail in this paper.

$$\frac{\partial^{2} p}{\partial t^{2}} = \frac{1}{\frac{\partial^{2}}{\partial x^{2}} + \frac{\partial^{2}}{\partial z^{2}}} \begin{pmatrix}
\widehat{\Psi}_{11} \begin{pmatrix} \zeta_{11} \left( -\nabla^{2} \right)^{\gamma_{11}} \\
-\chi_{11} \frac{\partial}{\partial t} \left( -\nabla^{2} \right)^{\gamma_{11} - \frac{1}{2}} \end{pmatrix} + \widehat{\Psi}_{33} \begin{pmatrix} \zeta_{33} \left( -\nabla^{2} \right)^{\gamma_{33}} \\
-\chi_{33} \frac{\partial}{\partial t} \left( -\nabla^{2} \right)^{\gamma_{33} - \frac{1}{2}} \end{pmatrix} \\
+ \Psi_{13} \begin{pmatrix} a_{1} \left( -\nabla^{2} \right)^{\mu_{33} \gamma_{33}} - b_{1} \frac{\partial}{\partial t} \left( -\nabla^{2} \right)^{\mu_{33} \gamma_{33} - \frac{1}{2}} \\
-a_{2} \left( -\nabla^{2} \right)^{\mu_{11} \gamma_{11}} + b_{2} \frac{\partial}{\partial t} \left( -\nabla^{2} \right)^{\mu_{11} \gamma_{11} - \frac{1}{2}} \end{pmatrix}
\end{pmatrix} P + f_{R}, \tag{9}$$

where  $f_R$  represent the recorded data. However, the high-frequency noise can occur during wavefield extrapolation, which will be exponentially amplified during the attenuation compensation process, resulting in instability in imaged results.

According to the theory of seismic wave propagation, the amplitude of seismic wave propagation in viscous media decays exponentially with the propagation distance (Mu et al., 2023; Mao

Subsequently, we adopt the HE-HFDPS numerical solution strategy to achieve high-efficiency and stable attenuation-compensated RTM. By using some mathematical derivations, the efficient and stable attenuation-compensated operator in the attenuation TTI media can be derived as follows (the detailed derivations see Appendix B):

$$\frac{\partial^{2} p}{\partial t^{2}} = \frac{1}{\frac{\partial^{2}}{\partial x^{2}} + \frac{\partial^{2}}{\partial z^{2}}} \begin{pmatrix}
\widehat{\Psi}_{11} \left( \zeta_{11}^{1} \left( -\nabla^{2} \right)^{\gamma_{11}} + \zeta_{11}^{2} \frac{\partial}{\partial t} \left( -\nabla^{2} \right)^{\gamma_{11}} + \zeta_{11}^{3} \frac{\partial}{\partial t} \left( -\nabla^{2} \right)^{\gamma_{11}+1} \right) \\
+ \widehat{\Psi}_{33} \left( \zeta_{33}^{1} \left( -\nabla^{2} \right)^{\gamma_{33}} + \zeta_{33}^{2} \frac{\partial}{\partial t} \left( -\nabla^{2} \right)^{\gamma_{33}} + \zeta_{33}^{3} \frac{\partial}{\partial t} \left( -\nabla^{2} \right)^{\gamma_{33}+1} \right) \\
- \left( \Psi_{1} \left( -\nabla^{2} \right)^{\mu_{33}\gamma_{33}} - \Psi_{2} \frac{\partial}{\partial t} \left( -\nabla^{2} \right)^{\mu_{33}\gamma_{33}-\frac{1}{2}} - \Psi_{3} \frac{\partial}{\partial t} \left( -\nabla^{2} \right)^{\frac{3}{2}\mu_{33}\gamma_{33}+\frac{\tau}{2}-1} \right) \\
+ \Psi_{13} \left( \xi_{1} \left( -\nabla^{2} \right)^{\mu_{11}\gamma_{11}} - \xi_{2} \frac{\partial}{\partial t} \left( -\nabla^{2} \right)^{\mu_{11}\gamma_{11}-\frac{1}{2}} - \xi_{3} \frac{\partial}{\partial t} \left( -\nabla^{2} \right)^{\frac{3}{2}\mu_{11}\gamma_{11}+\frac{\tau}{2}-1} \right)
\end{pmatrix}$$
(11)

et al., 2024a). Then, the analytical expression of amplitude compensation for seismic waves propagating in isotropic attenuation media can be written as

$$\begin{array}{lll} \text{where} & \zeta_{ij}^1 = & C_{ij}^{(\gamma_{ij}+1)} \omega_0^{-2\gamma_{ij}} \cos^{2\gamma_{ij}}(\frac{\pi\gamma_{ij}}{2}), & \zeta_{ij}^2 = & -2 \Upsilon_{ij} C_{ij}^{(\gamma_{ij}+1)} \omega_0^{-2\gamma_{ij}} \\ \cos^{2\gamma_{ij}}(\frac{\pi\gamma_{ij}}{2}) \tan(\frac{\pi\gamma_{ij}}{2}), & \zeta_{ij}^3 = & 2\tau \Upsilon_{ij} C_{ij}^{(\gamma_{ij}/2+1.5)} \cos^{\gamma_{ij-1}}(\frac{\pi\gamma_{ij}}{2}) \tan(\frac{\pi\gamma_{ij}}{2}) \omega_0^{-\gamma_{ij}}, \end{array}$$

L. Xiang, J.-P. Huang, Q. Mao et al.

$$\psi_i = \left(\zeta_{13}^i\right)^2 \left(\sqrt{\zeta_{11}^i \zeta_{33}^i}\right)^{-1}$$
, and  $\xi_i = \sqrt{\zeta_{11}^i \zeta_{33}^i}$ . Similar to the derivation of Eq. (7), we can obtain the efficient

Similar to the derivation of Eq. (7), we can obtain the efficient and stable attenuation-compensated extrapolation equation using the HE-HFDPS strategy as follows:

$$I^{c}(\mathbf{x}) = \frac{\int_{0}^{T} S^{a}(\mathbf{x}, t) R^{c}(\mathbf{x}, t) dt}{\int_{0}^{T} S^{a}(\mathbf{x}, t) S^{a}(\mathbf{x}, t) dt} = \frac{\int_{0}^{T} S(\mathbf{x}, t) R(\mathbf{x}, t) dt}{\int_{0}^{T} S(\mathbf{x}, t) S(\mathbf{x}, t) dt},$$
(13)

$$\begin{split} \frac{\partial^{2}p}{\partial t^{2}} &= -\hat{\Psi}_{11} \begin{pmatrix} \zeta_{11}^{1} \left( \dot{L}_{9}^{\prime} + 2\gamma_{11}(x) \dot{L}_{10}^{\prime} + 2\gamma_{11}^{2}(x) \dot{L}_{11}^{\prime} \right) + \zeta_{11}^{2} \left( \dot{L}_{12}^{\prime} + 2\gamma_{11}(x) \dot{L}_{13}^{\prime} + 2\gamma_{11}^{2}(x) \dot{L}_{14}^{\prime} \right) \\ &+ \zeta_{11}^{3} \left( \dot{L}_{15}^{\prime} + 2\gamma_{11}(x) \dot{L}_{16}^{\prime} + 2\gamma_{11}^{2}(x) \dot{L}_{17}^{\prime} \right) \\ &- \hat{\Psi}_{33} \begin{pmatrix} \zeta_{33}^{1} \left( \dot{L}_{9}^{\prime} + 2\gamma_{33}(x) \dot{L}_{10}^{\prime} + 2\gamma_{33}^{2}(x) \dot{L}_{11}^{\prime} \right) + \zeta_{33}^{2} \left( \dot{L}_{12}^{\prime} + 2\gamma_{33}(x) \dot{L}_{13}^{\prime} + 2\gamma_{33}^{2}(x) \dot{L}_{14}^{\prime} \right) \\ &+ \zeta_{33}^{3} \left( \dot{L}_{15}^{\prime} + 2\gamma_{33}(x) \dot{L}_{16}^{\prime} + 2\gamma_{33}^{2}(x) \dot{L}_{17}^{\prime} \right) \\ &- \psi_{13} \begin{pmatrix} \Psi_{1} \left( \dot{L}_{9}^{\prime} + 2_{2} \lambda_{33} \gamma_{33}(x) \dot{L}_{10}^{\prime} + 2(\lambda_{33} \gamma_{33}(x))^{2} \dot{L}_{11}^{\prime} \right) \\ &+ \Psi_{2} \left( \dot{L}_{12}^{\prime} + 2\lambda_{33} \gamma_{33}(x) \dot{L}_{13}^{\prime} + 2(\lambda_{33} \gamma_{33}(x))^{2} \dot{L}_{17}^{\prime} \right) \\ &- \begin{pmatrix} \xi_{1} \left( \dot{L}_{9}^{\prime} + 2\lambda_{11} \gamma_{11}(x) \dot{L}_{10}^{\prime} + 2(\lambda_{11} \gamma_{11}(x))^{2} \dot{L}_{11}^{\prime} \right) \\ &- \begin{pmatrix} \xi_{1} \left( \dot{L}_{9}^{\prime} + 2\lambda_{11} \gamma_{11}(x) \dot{L}_{13}^{\prime} + 2(\lambda_{11} \gamma_{11}(x))^{2} \dot{L}_{14}^{\prime} \right) \\ &+ \xi_{2} \left( \dot{L}_{12}^{\prime} + 2\lambda_{11} \gamma_{11}(x) \dot{L}_{16}^{\prime} + 2(\lambda_{11} \gamma_{11}(x))^{2} \dot{L}_{17}^{\prime} \right) \end{pmatrix} \end{pmatrix} + f, \end{split}$$

where  $L'_9 - L'_{17}$  are shown in Appendix C.

Compared to the traditional HFDPS strategy Eq. (C.2), which requires 17 FFTs ( $L_1'-L_{17}'$ ) per time step (the derivation is shown in Appendix C), the proposed HE-HFDPS numerical solution strategy only retains 9 FFTs ( $L_9'-L_{17}'$ ), reducing the number of FFTs from 17 to 9 per time step during Q-compensated RTM. That demonstrates that the proposed HE-HFDPS numerical solution strategy has significant potential for improved computational efficiency in Q-compensated RTM.

For attenuation anisotropic media, the Q-compensated RTM workflow involves three steps. To describe the amplitude attenuation, we assume the exponential form  $e^{-\eta(\theta)L}$ , where L represents the propagation distance,  $\eta(\theta)$  denote the attenuation factor. Firstly, based on the pure viscoacoustic TTI wave propagation Eq. (6) to simulate the forward source wavefield. This process can be expressed mathematically as  $S^{a}(\mathbf{x},t) = S(\mathbf{x},t)e^{-\eta(\theta)L_{\text{down}}}$ . Secondly, by using the stable attenuation-compensated extrapolation Eq. (11) as the reverse-time wavefield extrapolation operator to realize the backward propagation of the seismic record that the process can be expressed as  $R^{c}(\mathbf{x},t) = R^{a}(\mathbf{x},t)e^{+\eta(\theta)L_{up}} = R(\mathbf{x},t)e^{-\eta(\theta)L_{down}}e^{-\eta(\theta)L_{up}}e^{+\eta(\theta)L_{up}}$  $\eta(\theta)L_{\rm up}=R({\bf x},t){\rm e}^{-\eta(\theta)L_{\rm down}}.$  Note that where  $S^{\rm a}({\bf x},t)$ ,  $R^{\rm a}({\bf x},t)$ , and  $R^{c}(\mathbf{x},t)$  represent the attenuation source, the attenuation receiver, and the compensated receiver wavefield, respectively,  $S(\mathbf{x},t)$ ,  $R(\mathbf{x},t)$ denote the forward propagation source and backward propagation receiver wavefields in non-attenuating media, respectively. Thirdly, applying a suitable imaging condition to obtain the final imaging results (Fathalian et al., 2021). The widely used source-normalized cross-correlation imaging condition can be expressed as

where *T* is the total time of the seismic recording. Eq. (13) shows that the imaging results of the compensated migration are theo-

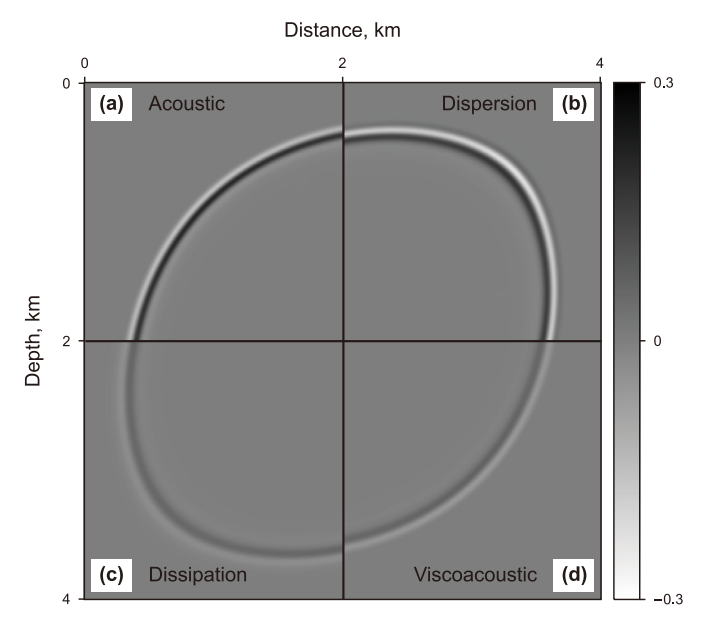


**Fig. 5.** Snapshots at 0.6 s were calculated using **(a)** acoustic TTI, **(b)** dispersion-dominant TTI, **(c)** dissipation-dominated TTI, and **(d)** viscoacoustic TTI wave equations, respectively. The model parameters are  $v_{\rm p}=3000$  m/s,  $\varepsilon=0.3$ ,  $\delta=0.1$ ,  $Q_{\rm p}=30$ ,  $\varepsilon_{\rm O}=0.4$ ,  $\delta_{\rm O}=-0.1$  and  $\phi=45^\circ$  at the reference frequency of 500 Hz.

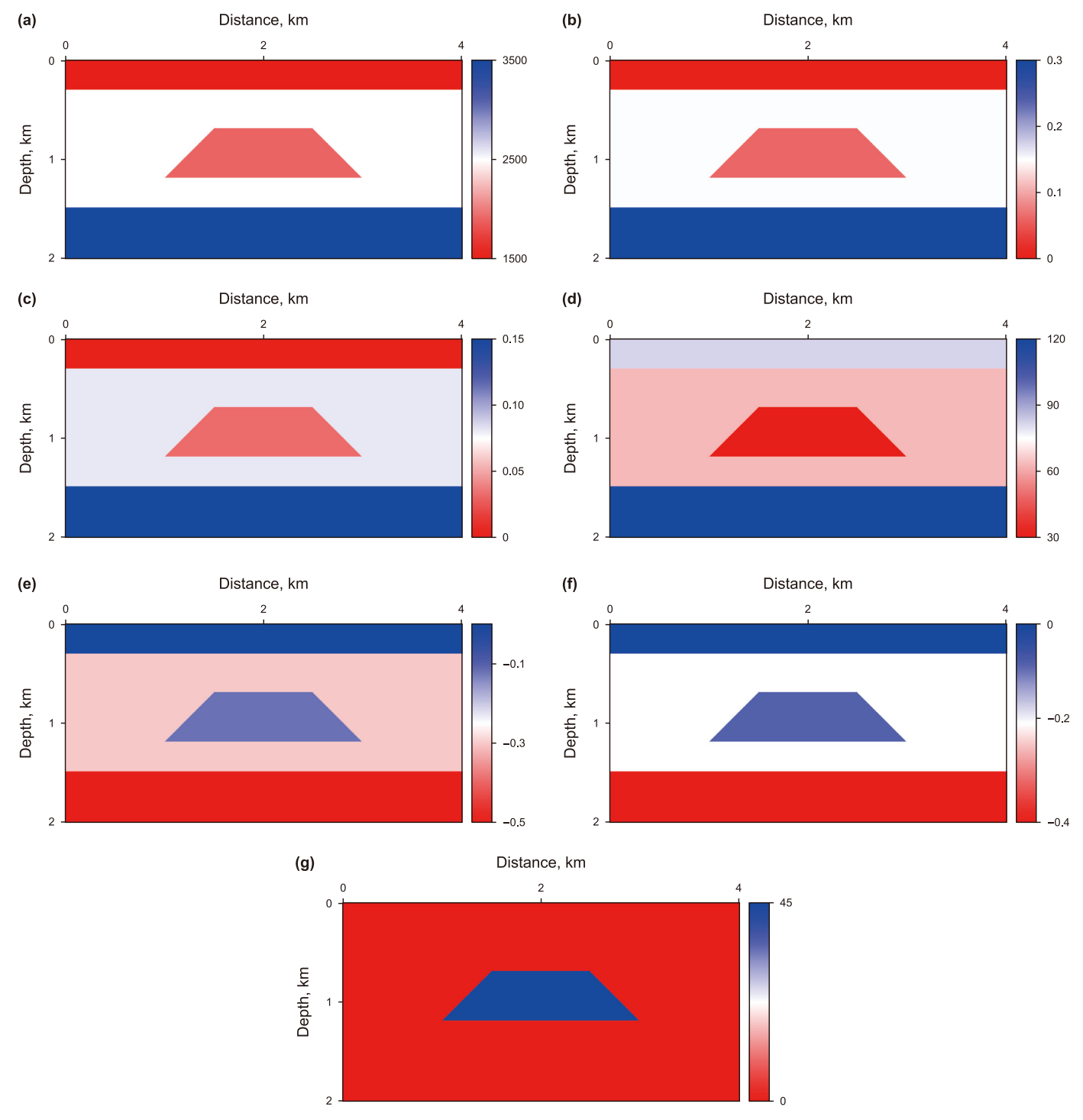


**Fig. 6.** Gas cloud model: (a)  $v_p$ , (b)  $\varepsilon$ , (c)  $\delta$ , (d)  $Q_p$ , (e)  $\varepsilon_Q$ , (f)  $\delta_Q$ , (g)  $\phi$ .

retically equivalent to the imaging results of the acoustic anisotropic migration.

#### 3. Numerical examples

In this section, we utilize the HFDPS strategy Eq. (4) proposed by Xiang et al. (2025) to produce the reference wavefield and compare it with the proposed HE-HFDPS numerical modeling strategy Eq. (7). Boundary reflections are suppressed by sponge-absorbing boundary conditions (Cerjan et al., 1985).

# 3.1. The dissipation and dispersion properties of the algebraic method

To demonstrate that the proposed HE-HFDPS numerical modeling strategy based on the algebraic method can simulate the separate effects of amplitude attenuation and phase dispersion, we construct a homogeneous model with a size of 401  $\times$  401, and the size of the vertical and horizontal grids is 10 m. A Ricker wavelet is located at (2010 m, 2010 m) as the source, and the peak frequency is 25 Hz. The time step for the numerical simulation is 1 ms. The

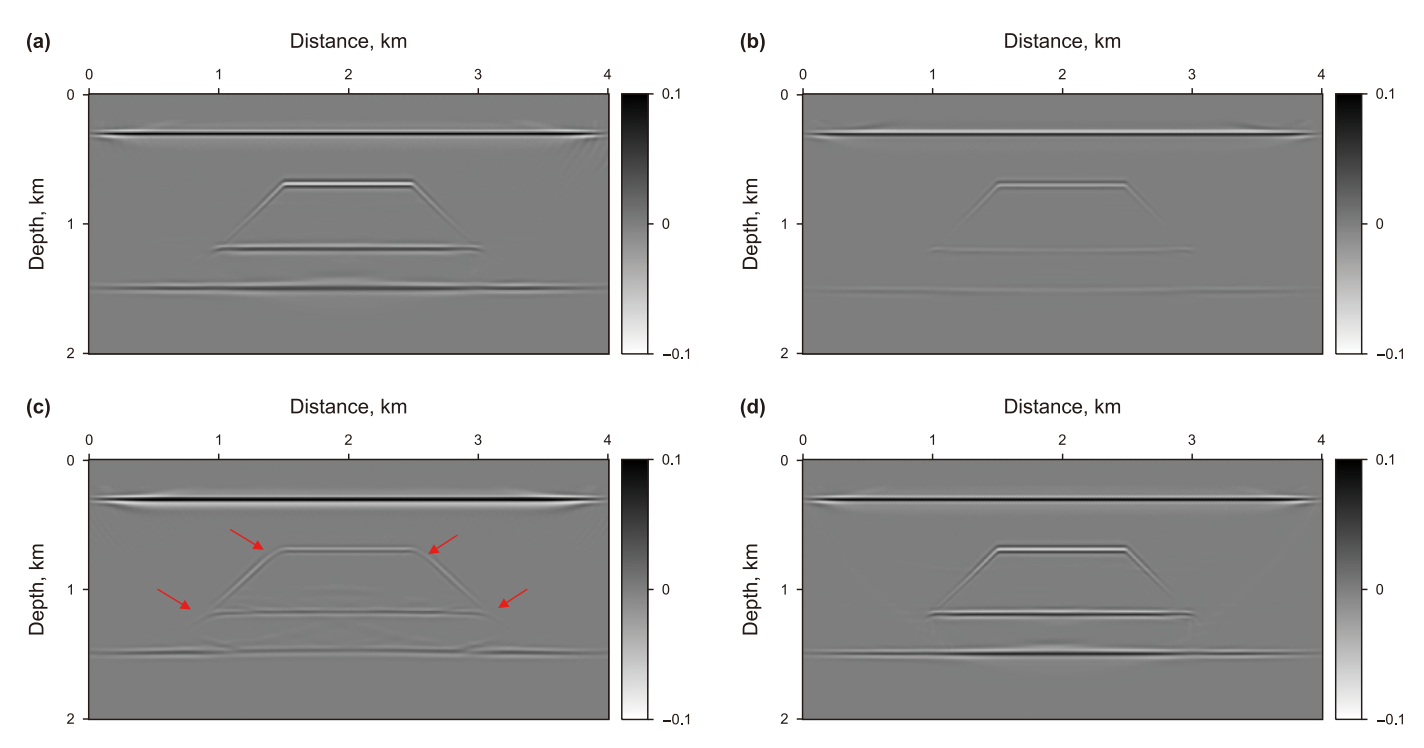
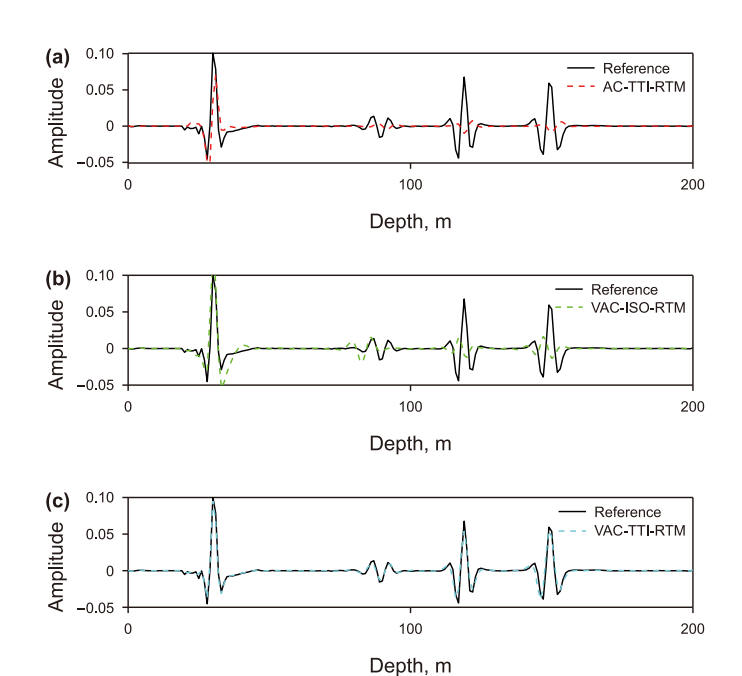


Fig. 7. Migration imaging results of (a) acoustic TTI data with acoustic-TTI RTM (reference), (b) viscoacoustic-TTI data with acoustic-TTI RTM, (c) viscoacoustic-TTI data with viscoacoustic-TTI RTM.



**Fig. 8.** Trace comparison from Fig. 7 at a horizontal distance of 1.3 km. The black solid line denotes the reference trace extracted from Fig. 7(a). **(a)** The red, **(b)** green, and **(c)** blue dashed lines represent the trace from Fig. 7(b), 7(c), and 7(d), respectively.

model parameters are  $v_p=3000$  m/s,  $\varepsilon=0.3$ ,  $\delta=0.1$ ,  $Q_p=30$ ,  $\varepsilon_Q=0.4$ ,  $\delta_Q=-0.1$  and  $\phi=45^\circ$  at the reference frequency of 500 Hz.

Fig. 5 shows snapshots at 0.6 s were calculated using acoustic TTI (Fig. 5(a)), dispersion-dominant TTI (Fig. 5(b)), dissipation-dominated TTI (Fig. 5(c)), and viscoacoustic TTI wave equations (Fig. 5(d)), respectively. As shown in Fig. 5(a) and (b), the amplitude

of the dispersion-dominated wavefield is similar to that of the acoustic wavefield, but the phase is delayed due to the velocity dispersion. In Fig. 5(c), the wavefront of the dissipative dominant wavefield is the same as that of the acoustic dominant wavefield, but the amplitude is reduced significantly. The simulated viscoacoustic wavefield has both attenuated amplitude and delayed phase in Fig. 5(d). This experiment shows that the proposed HE-HFDPS numerical modeling strategy based on the algebraic method can achieve a decoupled wave field simulation of amplitude attenuation and phase dispersion, which is beneficial for implementing *Q*-compensated RTM in attenuated anisotropic media.

## 3.2. A simple gas reservoir model

To illustrate the influence of viscosity and anisotropy on migration imaging of the proposed efficient and stable attenuation-compensated RTM scheme, we construct a simple gas cloud model. The model parameters and structure are shown in Fig. 6 with a grid size of  $401 \times 201$  for the numerical experiments, and the vertical and horizontal grid spacing is 10 m. The time step for the numerical simulation is 0.8 ms, and the total recording time is 2.4 s. We located 80 shots at a depth of 10 m as the source, the shot spacing is 50 m. The peak frequency is 25 Hz and the reference frequency is 500 Hz. We used 401 surface-deployed receivers to record the reflections for each shot, with a receiver interval of 10 m. Notice that the acoustic TTI shot is gathered by assuming  $Q \rightarrow \infty$  in Eq. (4) and the  $\omega_{\tau} = 70\pi$  rad/s.

In Fig. 7, we present the acoustic-TTI RTM (AC-TTI RTM) result obtained by using acoustic-TTI data as the reference (Fig. 7(a)), the AC-TTI RTM imaging result computed by using viscoacoustic (VA) data in Fig. 7(b), the viscoacoustic-ISO RTM (VA-ISO RTM) result calculated by using viscoacoustic data in Fig. 7(c), and the viscoacoustic-TTI RTM (VA-TTI RTM) imaging result by using viscoacoustic data in Fig. 7(d), respectively. Upon comparing

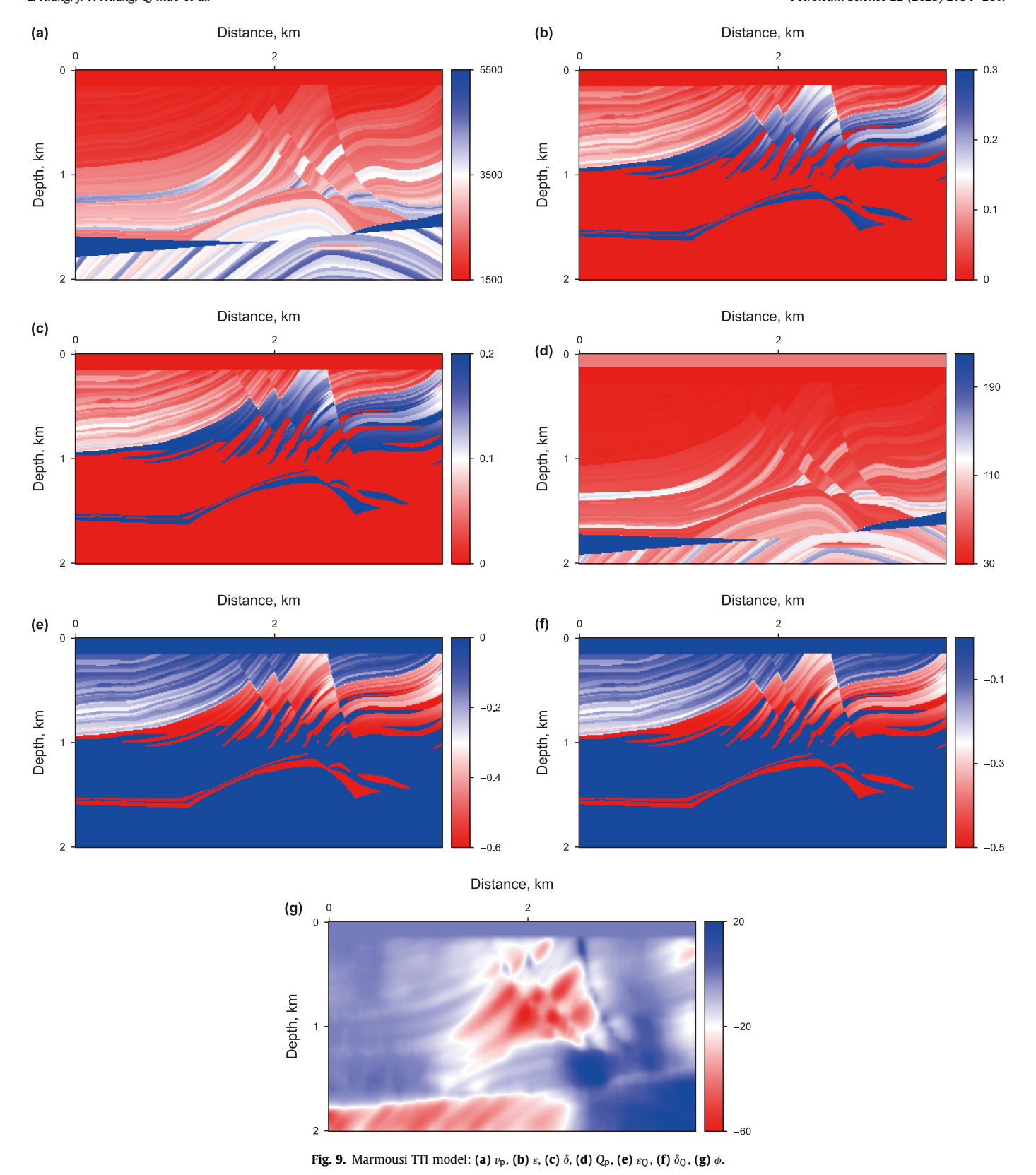


Fig. 7(b)—(a), the AC-TTI RTM result computed by using viscoacoustic data exhibits amplitude energy attenuation because of ignoring the viscosity effect. Analysis of Fig. 7(c) reveals that the amplitude energy of the VA-ISO RTM result is compensated. However, the deep structures remain unrecovered and exhibit

obvious phase distortion because the anisotropic effect is ignored (as shown by the red arrow in Fig. 7(c)). It is evident from Fig. 7(d) that the amplitude energy is well compensated.

For a more detailed comparison, Fig. 8 shows the vertical profiles at horizontal distances of 1.3 km extracted from Fig. 7. In

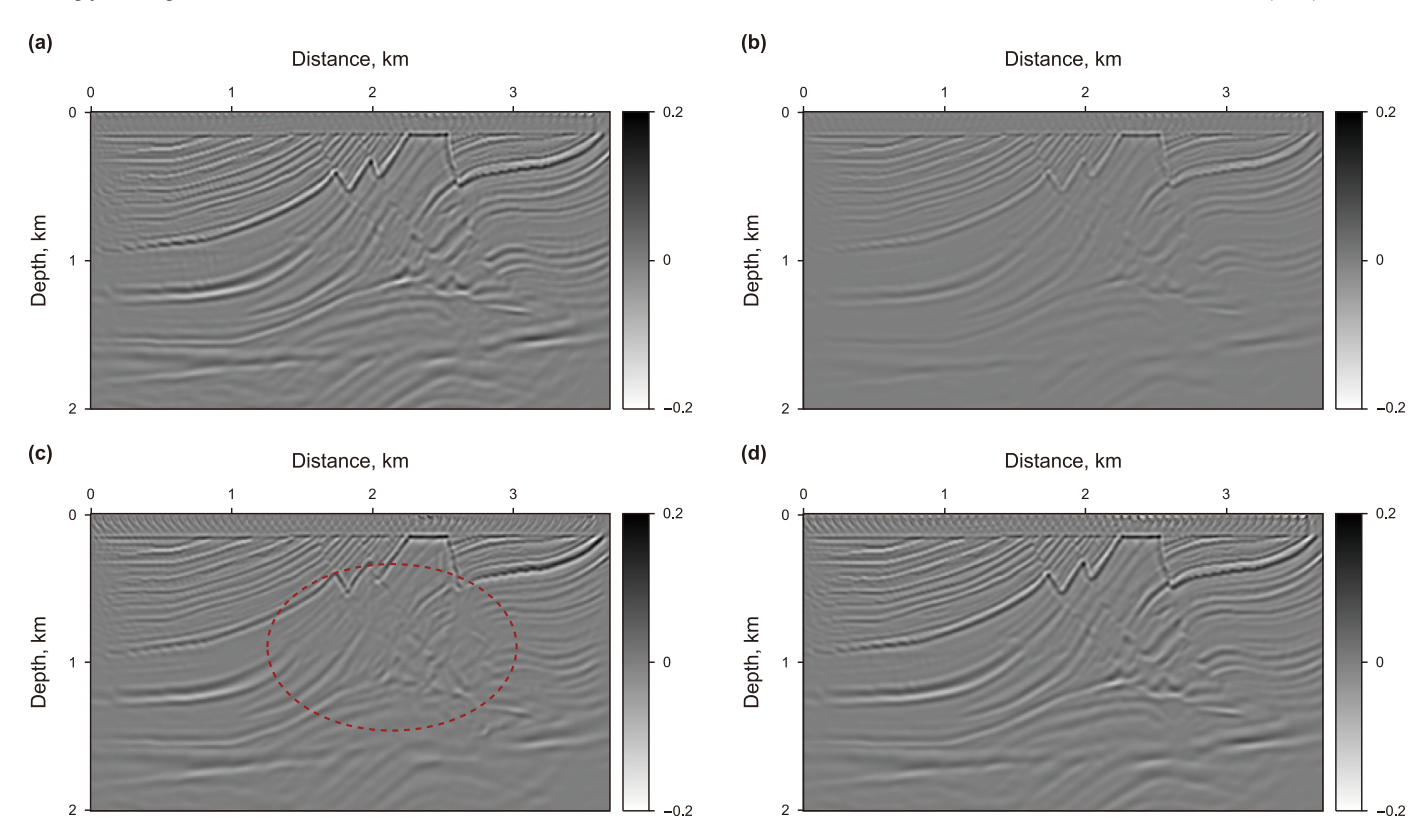
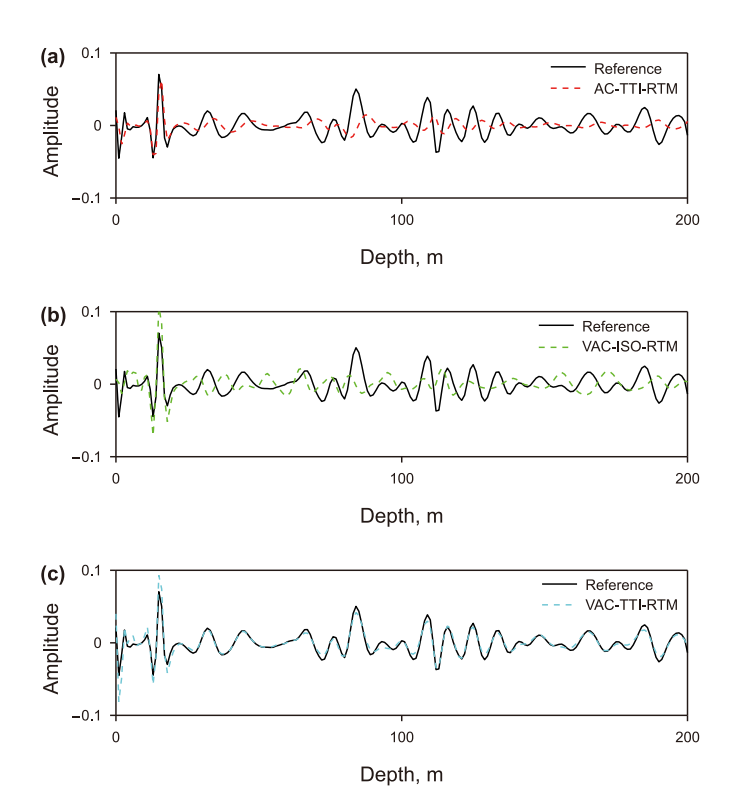


Fig. 10. Migration imaging results of Marmousi TTI model. (a) Acoustic TTI data with acoustic-TTI RTM (reference), (b) viscoacoustic-TTI data with acoustic-TTI RTM, (c) viscoacoustic-TTI data with viscoacoustic-ISO RTM, and (d) viscoacoustic-TTI data with viscoacoustic-TTI RTM.



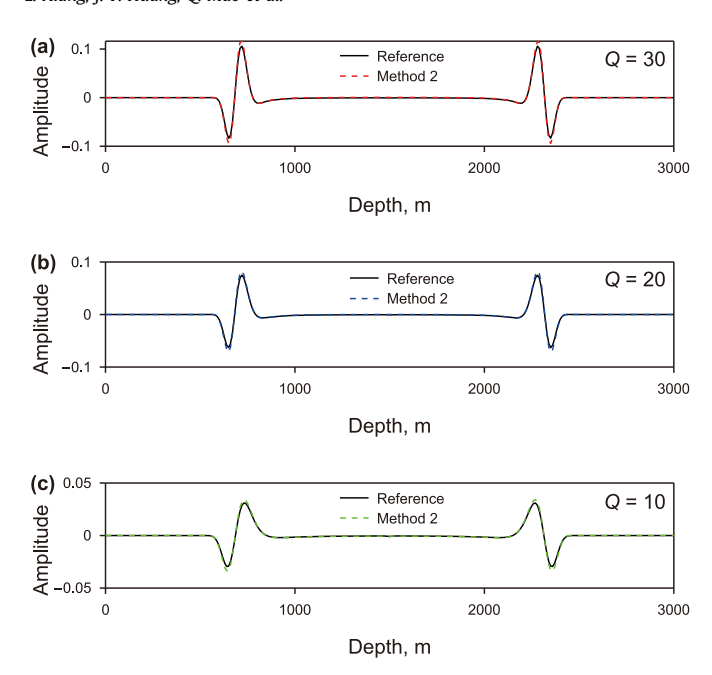
**Fig. 11.** Trace comparison from Fig. 10 at a horizontal distance of 2.3 km. The black solid line denotes the reference trace extracted from Fig. 10(a). (a) The red, (b) green, and (c) blue dashed lines represent the trace from Fig. 10(b), 10(c), and 10(d), respectively.

Fig. 8(a), the red dotted line exhibits a weak amplitude and a significant phase shift compared to the reference traces (the black solid line). In Fig. 8(b), the green dashed line compensates for the amplitude in the shallow layers, however, the amplitude in the deeper layers remains weak and displays a significant phase shift. Analyzing Fig. 8(c), the blue dotted line agrees very well with the black solid lines. The above numerical examples show that the newly derived *Q*-compensated TTI RTM based on the algebraic method can simultaneously correct waveform distortion and amplitude weaker caused by anisotropy and attenuation.

## 3.3. Modified Marmousi TTI model

To demonstrate the practicality of the new stable Q-compensated RTM method in a complex geological model, we created a modified attenuation Marmousi model in Fig. 9. The model has a grid size of  $369 \times 201$  with vertical and horizontal grid spacings of 10 m. The time step for the numerical simulation is 0.8 m, and the total recording time is 2.4 s. We used a Ricker wavelet with a dominant frequency of 20 Hz as the source, with a reference frequency of 500 Hz. There are 61 shots positioned at a depth of 10 m, with a shot spacing of 60 m. We employed 369 surface-deployed receivers, positioned at 10 m intervals, to record the reflections for each shot. Notice that  $\omega_{\rm T}=70\pi$  rad/s.

In Fig. 10, we plotted the reference RTM imaging (Fig. 10(a)), the AC-TTI RTM result (Fig. 10(b)), the VA-ISO RTM imaging result (Fig. 10(c)), and the VA-TTI RTM result (Fig. 10(d)). Additionally, in Fig. 11, we provided a more detailed comparison by showing the vertical profiles at horizontal distances of 2.3 km extracted from the results in Fig. 10. From Fig. 10(b)—(a), we observed that the AC-TTI RTM result computed by using viscoacoustic data exhibited amplitude energy attenuation and phase distortion when

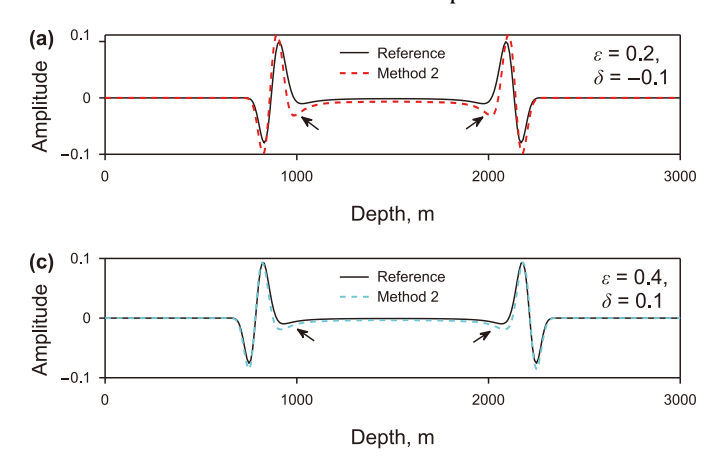


**Fig. 12.** Trace comparison at a horizontal distance of 0.8 km. The black solid line and dashed line are the wavefield traces computed by the reference HFDPS strategy Eq. (4) and the proposed HFDPS strategy Eq. (C.9) based on the asymptotic approximation method for the quality factors Q = 30 (a), Q = 20 (b), and Q = 10 (c), respectively.

comparing the reference results. In Figs. 10(c) and 11(d), the VA-ISO RTM results not only showed poor amplitude energy compensation but also significant phase distortion (as shown by the black circles). However, the amplitude energy of the VA-TTI RTM result is compensated, and the phase is corrected well in Figs. 10(d) and 11(c). The above synthetic examples indicate that the newly derived *Q*-compensated TTI RTM using the algebraic method can simultaneously correct waveform distortion and amplitude weaker caused by anisotropy and attenuation in complex attenuation media.

#### 4. Discussions

In the above section, we proposed a new HE-HFDPS numerical modeling strategy based on the algebraic method, which has no approximation and only algebraic operations compared with the reference equation. In this section, we discuss another HE-HFDPS numerical modeling strategy based on the asymptotic approximation method to further reduce the computation number of FFTs



per time step. Similar to the asymptotic approximation method used in anisotropic non-attenuation forward modeling by Xu and Zhou (2014). We extend the use of the asymptotic approximation ( $\mathbf{n} = \mathbf{k}/|\mathbf{k}| = \nabla P/|\nabla P|$ ) from anisotropic acoustic media into anisotropic attenuation media to eliminate the fractional form  $\frac{1}{k_x^2+k_z^2}$  of the correction term. This method only retains  $(L_1-L_5)$  compared to the traditional strategy Eq. (4)  $(L_1-L_{11})$ , reducing the number of FFTs from 11 to 5 per time step. In addition, the asymptotic approximation method does not contain any fourth-order partial derivatives, only second-order partial derivatives, further improving the computational efficiency. The detailed derivation is shown in Appendix D.

However, the asymptotic approximation will lead to the imbalance of the propagation amplitudes in different directions. When using a scalar operator for the correction term in an attenuation anisotropic media, this amplitude imbalance caused by the asymptotic approximation method is coupled to the influence of the attenuation anisotropy. It is difficult to distinguish whether the change in amplitude is due to the characteristics of the attenuation anisotropy or to an error in the approximation method. Fortunately, the asymptotic approximation retains relatively accurate phase information, although slight phase variations occur due to amplitude imbalances. In addition, the phase and amplitude characteristics of the wavefield are mainly affected by the elliptic term in the approximate complex-valued dispersion relation (Xu et al., 2015). Thus, when we use an approximation only for the propagation direction of the correction term, this approximation will yield unbalanced amplitude energy but still can characterize the features of attenuation anisotropy in attenuation TTI media. Compared with the improved computational efficiency, part of the accuracy loss is acceptable for numerical modeling in attenuated TTI media, especially for Q-compensated RTM. To analyze the effect of the asymptotic approximation on forward modeling and Qcompensated RTM, we will provide several analytical and numerical simulation examples in the following section.

Recent studies on anisotropic media have shown that replacing the scalar operator with the optical flow method (Zhang et al., 2024), in conjunction with constructing the multi-propagating components of the equation, can effectively mitigate the wave-field propagation energy imbalance typically caused by the scalar operator. In future research, we plan to explore the integration of the optical flow method into attenuating anisotropic media to address the limitations of the scalar operator. This approach may provide an effective solution to the challenges associated with wavefield propagation in such media.

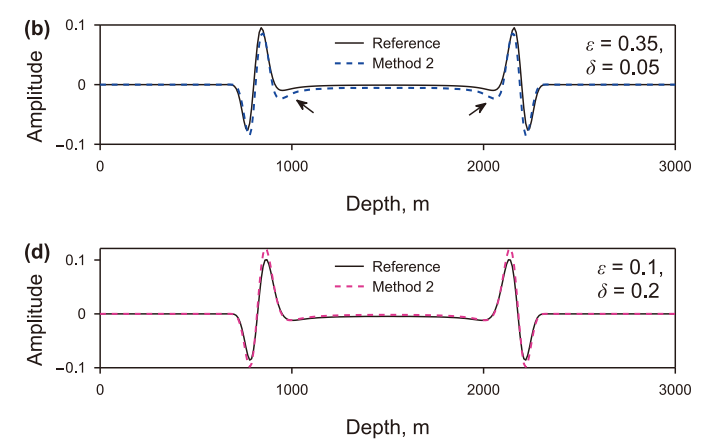


**Fig. 13.** Trace comparison at a horizontal distance of 0.8 km. The black solid line and dashed line are the wavefield traces computed by the reference HFDPS strategy Eq. (4) and the proposed HFDPS strategy based on the asymptotic approximation method (Method 2) Eq. (C.9) for the Thomson anisotropy parameters  $\varepsilon = 0.2$ ,  $\delta = -0.1$  ( $\eta = 0.375$ ) (a),  $\varepsilon = 0.35$ ,  $\delta = 0.05$  ( $\eta = 3/8$ ) (b),  $\varepsilon = 0.4$ ,  $\delta = 0.1$  ( $\eta = 0.25$ ) (c), and  $\varepsilon = 0.1$ ,  $\delta = 0.2$  ( $\eta = -1/14$ ) (d), respectively.

# 4.1. Numerical simulation analysis of asymptotic approximation method

To analyze the effect of the asymptotic approximation method on attenuation and phase, we designed two types of models to be compared separately. First, to assess the influence of the attenuation, we assume the Thomsen anisotropic parameters  $\varepsilon = 0.2$ ,  $\delta =$ 0.15. and the attenuation anisotropic parameters  $\varepsilon_{\rm Q}=0.2$ ,  $\delta_{\rm Q}=$ 0.15 to eliminate the effects of the velocity anisotropic and attenuation anisotropic. The other parameters are the same as in Section 2.3. In Fig. 12, we plot comparisons of the wavefield tracks at a horizontal distance of 0.8 km computed using the reference wave Eq. (4) (the black solid line) and the asymptotic approximation method Eq. (D.9) (the dotted line) for the quality factors Q = 30 (Fig. 12(a)), Q = 20 (Fig. 12(b)), and Q = 10 (Fig. 12(c)), respectively. In Fig. 12, when the effect of anisotropy is small, the difference between the wavefield snapshots tracks comparisons of dotted lines and the black solid line for different quality factor conditions is small. It proves that the computational error of this approximation is not highly sensitive to the variation of the attenuation characteristics.

Subsequently, to analyze the influence of the anisotropic parameters, we assume the quality factor Q = 30 and the anisotropic attenuation parameters  $\varepsilon_{\rm O}=$  0.2,  $\delta_{\rm O}=$  0.15. In Fig. 13, we show a comparison of the wavefield tracks at a horizontal distance of 0.8 km computed by the reference wave (the black solid line) and the asymptotic approximation method (the dotted line) for the Thomsen anisotropic parameter  $\varepsilon = 0.2$ ,  $\delta = -0.1$  ( $\eta = 0.375$ ) (Fig. 13(a)),  $\varepsilon = 0.35$ ,  $\delta = 0.05$  ( $\eta = 3/8$ ) (Fig. 13(b)),  $\varepsilon = 0.4$ ,  $\delta = 0.1$  $(\eta = 0.25)$  (Fig. 13(c)), and  $\varepsilon = 0.1$ ,  $\delta = 0.2$   $(\eta = -1/14)$ (Fig. 13(d)), respectively. Notice that  $\eta = (\varepsilon - \delta)/(1 + 2\delta)$  is dimensionless anisotropy parameters used to describe the anellipticity of anisotropic media (Alkhalifah, 1998). From Fig. 13, we can see that as the parameter  $\eta$  increases, the effects of amplitude unbalance between the track computed by using the asymptotic approximation and the reference track increases (as shown in the black arrow). However, the phase information of the simulated wavefields in Fig. 13 is relatively accurate, although there are variations in phase due to amplitude imbalances. This analysis indicates that the influence of the asymptotic approximation method on the wavefield phase and amplitude increases as the anellipticity of the anisotropic medium increases, but has relatively accurate phase information. In addition, we can find that even when the anellipticity parameter  $\eta = 0.25$ , the phase and amplitude information are relatively accurate (Fig. 13(c)). Since most bulk elastic media are weakly anisotropic (Thomsen, 1986), the anellipticity parameter  $\eta$ is generally less than 0.25. Therefore, the asymptotic approximation method is effective for common weakly anisotropic media.

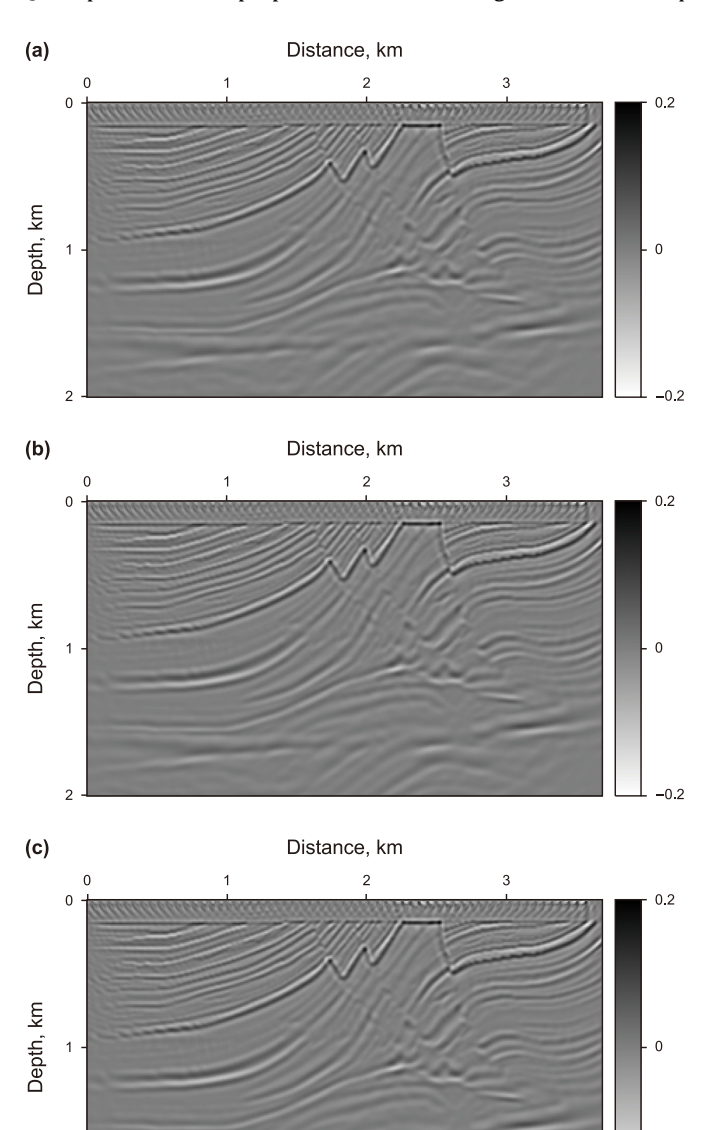
# 4.2. Comparison of Q-compensated RTM results of different numerical simulation methods

To compare the application of the algebraic and the asymptotic approximation methods in *Q*-compensated RTM. We use the same shot data result calculated by the reference pure viscoacoustic TTI wave Eq. (4). The Marmousi model and observation system parameters are the same as in Section 3.3. In Fig. 14, we show the *Q*-compensated RTM result calculated by the reference attenuation-compensated modeling Eq. (D.2) (Fig. 14(a)), the *Q*-compensated RTM result computed by the HE-HFDPS based on the algebraic method Eq. (12) (Fig. 14(b)), the *Q*-compensated RTM result calculated by the HE-HFDPS based on the asymptotic approximation method Eq. (D.10) (Fig. 14(c)), respectively. Fig. 14 shows that these numerical modeling methods can stably image model structures and obtain relatively accurate results. For a more detailed

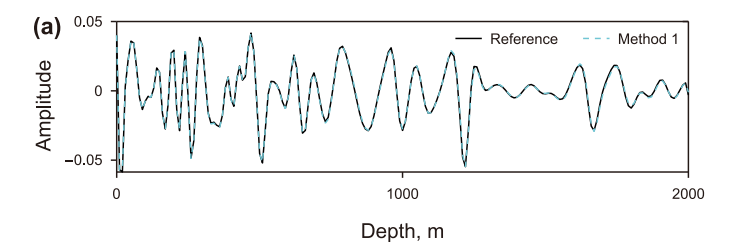
comparison, Fig. 15 shows the vertical profiles at horizontal distances of 2.6 km extracted from Fig. 14. In Fig. 15(a), the blue dashed line (algebraic method results) is close to the black solid line and almost overlaps. However, the migration results obtained by the asymptotic approximation method (red dotted line) have slight amplitude differences and phase distortion compared with the reference results (as indicated by the black arrow). The above imaging results demonstrate that the algebraic method has higher simulation accuracy than the asymptotic approximation method, which can be well applied to attenuation compensation RTM.

## 4.3. Analysis of attenuation compensation methods

To compare the proposed stabilization method with the lowpass filtering method in suppressing random noise, we take the Q-compensated RTM proposed based on the algebraic method Eq.



**Fig. 14.** Migration imaging results of the Marmousi model. **(a)** Q-compensated RTM result computed by the reference attenuation-compensated modeling Eq. (B.2) (reference), **(b)** the Q-compensated RTM result calculated by the attenuation-compensated modeling Eq. (11) based on the algebraic method, and **(c)** the Q-compensated RTM result computed by the attenuation-compensated modeling Eq. (C.1) based on the asymptotic approximation method.



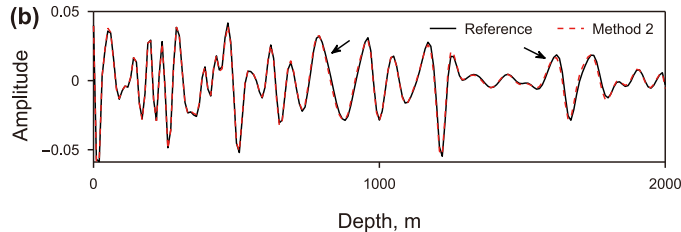


Fig. 15. Trace comparison from Fig. 14(a). (a) The blue and (b) red dashed lines represent the trace from Fig. 14(b) and (c), respectively. Method 1 and Method 2 represent the algebraic and asymptotic approximation methods, respectively.

(12) as an example and introduce Gaussian random noise into the improved Marmousi TTI model (Fig. 9). The signal-to-noise ratios (S/N) of the gathers are 10 dB and 5 dB, respectively. Notice that the cutoff frequency for the low-pass filter is set to 70 Hz and the parameters are the same as in Section 3.3.

In Fig. 16, the imaging results obtained by using the *Q*-compensated RTM based on the algebraic method Eq. (12) (Fig. 16(a)—(c)) and the traditional *Q*-compensated RTM using the low-pass filtering method (Fig. 16(b)—(d)), respectively. It can be seen from Fig. 16 that both the traditional and the newly proposed *Q*-compensated RTM can produce stable imaging results. As the S/N ratio decreases, the noise in the imaging results gradually increases. Compared with the traditional RTM imaging results using low-pass filters (Fig. 16(b)—(d)), the RTM imaging results based on the stability factor method (Fig. 16(a)—(c)) have lower noise and higher resolution. Especially when the S/N ratio is 5, the fault zone structure in the traditional *Q*-compensated RTM using the low-pass filter is obscured by strong noise (as indicated by the red dotted ellipse and arrows). In contrast, the fault zone structure remains visible in the imaging results obtained with the proposed *Q*-

compensated RTM using the stability factor method. This shows that the proposed *Q*-compensated RTM based on stability factor is superior to the traditional *Q*-compensated RTM using the low-pass filter in suppressing high-frequency noise.

#### 5. Conclusions

We have proposed two HE-HFDPS numerical modeling strategies based on the asymptotic approximation and the algebraic methods to discretize the fractional Laplacian pure viscoacoustic wave equation, respectively. Based on the algebraic method, the new HE-HFDPS strategy reduces the number of FFTs from 11 to 6 per time step in forward modeling. For Q-compensated RTM, only 9 FFTs per time step are retained compared to the traditional strategy of 17 FFTs. In addition, it does not use any additional approximation, so the wavefield simulation accuracy of this scheme is equivalent to that of the original HFDPS numerical modeling strategy. Using the asymptotic approximation method, the other HE-HFDPS strategy cuts the number of FFTs from 11 to 5 per time step in forward modeling and only retains 8 FFTs per time step during Q-

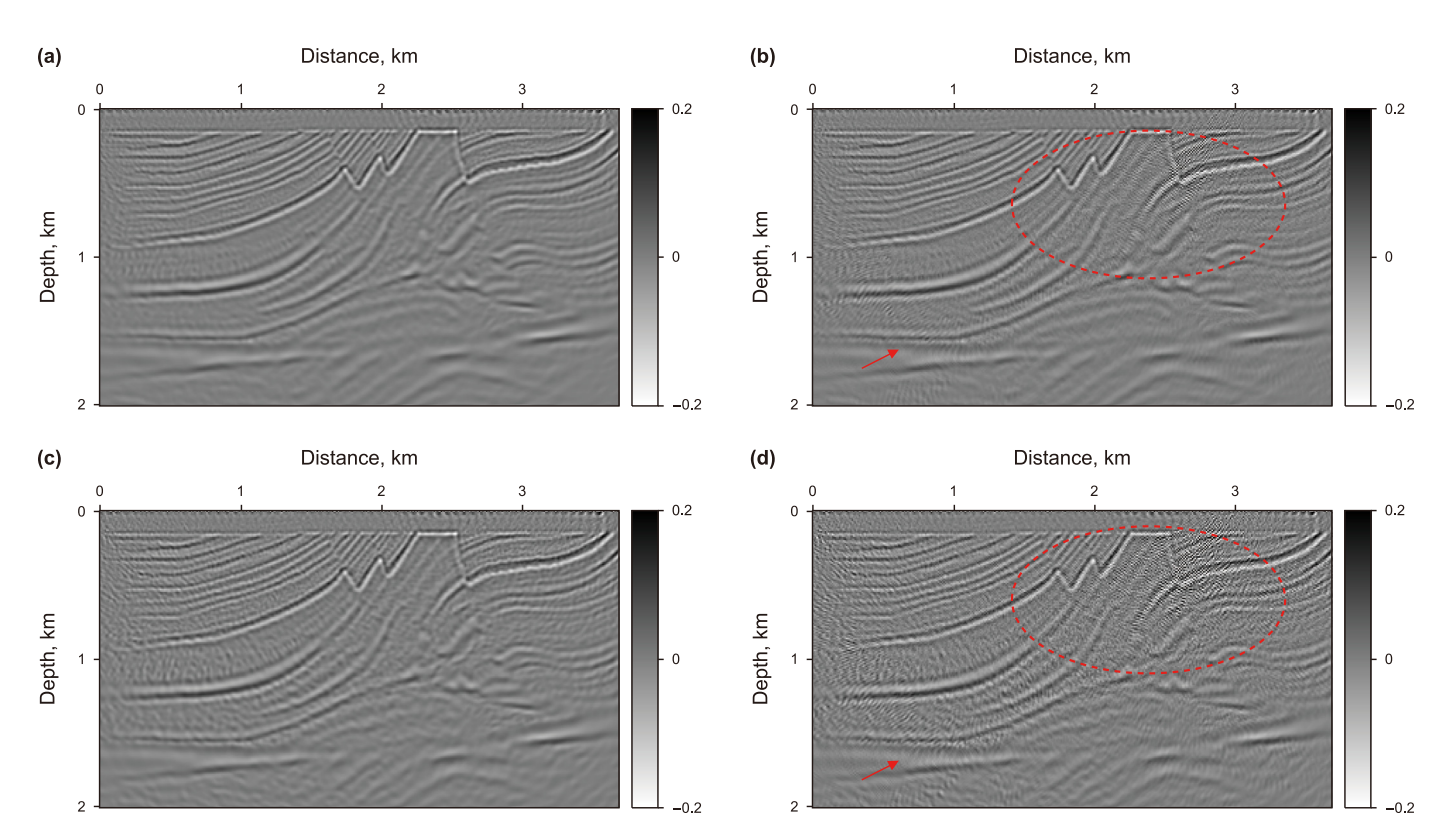


Fig. 16. Migration results by using the stabilization factor *Q*-compensated TTI RTM ((a), (c)) and the Low-pass filter *Q*-compensated TTI RTM ((b), (d)). The S/Ns of the used gathers are 10 dB ((a)–(b)), 5 dB ((c)–(d)), respectively. Notice the cutoff frequency for the low-pass filter is 70 Hz.

compensated RTM, further improving computational efficiency. However, it exhibits phase distortions and amplitude imbalances. Then, based on the HE-HFDPS strategies, we derived efficient and stable attenuation-compensated extrapolation operators and implemented the Q-compensated RTM in the attenuation TTI media. The synthetic data results demonstrate that the proposed Ocompensated TTI RTM method effectively corrects and compensates for waveform distortion and amplitude attenuation induced by anisotropy and attenuation. Additionally, the HE-HFDPS strategy significantly improves computational efficiency, achieving nearly double the performance of traditional methods, thereby greatly enhancing seismic imaging and inversion capabilities. As a result, this method contributes to more accurate subsurface imaging and provides strong support for resource exploration and monitoring in complex geological environments, such as fractured reservoirs and salt structures. These advancements highlight the significant potential for widespread application in practical seismic data processing.

#### **CRediT authorship contribution statement**

**Lei Xiang:** Writing — original draft, Visualization, Validation, Software, Methodology, Formal analysis, Data curation. **Jian-Ping Huang:** Writing — original draft, Validation, Supervision. **Qiang Mao:** Writing — original draft, Validation, Supervision. **Xin-Ru Mu:** 

contract number 41821002, and the basic theoretical research of seismic wave imaging technology in complex oilfield of Changqing Oilfield Company under contract number 2023—10502.

#### APPENDIX A

Derivation of the fractional Laplacian pure viscoacoustic wave equation.

According to Eq. (1), The approximate dispersion relation is represented as

$$\omega^{2} \approx M_{11}k_{x}^{2} + M_{33}k_{z}^{2} + \frac{\left(M_{13}^{2}\left(\sqrt{M_{11}M_{33}}\right)^{-1} - \sqrt{M_{11}M_{33}}\right)k_{x}^{2}k_{z}^{2}}{k_{x}^{2} + k_{z}^{2}},$$
(A.1)

where  $k_x,k_z$  denote spatial wavenumbers along the horizontal and vertical directions, respectively. To transform Eq. (A.1) into TTI media, we insert the coordinate rotation relations  $\widehat{k}_x = \cos\phi k_x - \sin\phi, \widehat{k}_z = \sin\phi k_x + \cos\phi k_z$  into Eq. (A.1), and replacing  $k_x^2$  and  $k_z^2$  with  $\widehat{k}_x^2$  and  $\widehat{k}_z^2$ . where  $\phi$  is the tilt angle. Then, the TTI approximated complex-valued dispersion relation can be expressed as

$$\omega^{2} \approx M_{11} \left( \sin^{2} \phi k_{z}^{2} + \cos^{2} \phi k_{x}^{2} - \sin 2 \phi k_{x} k_{z} \right)$$

$$+ M_{33} \left( \sin^{2} \phi k_{x}^{2} + \cos^{2} \phi k_{z}^{2} + \sin 2 \phi k_{x} k_{z} \right)$$

$$+ \frac{M_{13}^{2} \left( \sqrt{M_{11} M_{33}} \right)^{-1} - \sqrt{M_{11} M_{33}}}{k_{x}^{2} + k_{z}^{2}} \begin{pmatrix} \sin^{2} \phi \cos^{2} \phi \left( k_{x}^{4} + k_{z}^{4} \right) \\ + \left( \cos^{4} \phi + \sin^{4} \phi - \sin^{2} 2 \phi \right) k_{x}^{2} k_{z}^{2} \\ + \sin 2 \phi \left( \cos^{2} \phi - \sin^{2} \phi \right) k_{x} k_{z}^{3} \end{pmatrix},$$

$$+ \sin 2 \phi \left( \sin^{2} \phi - \cos^{2} \phi \right) k_{x} k_{z}^{3}$$

$$+ \sin 2 \phi \left( \sin^{2} \phi - \cos^{2} \phi \right) k_{x} k_{z}^{3}$$

$$(A.2)$$

Writing — original draft, Validation, Supervision. **Fei Li:** Project administration, Funding acquisition. **Juan Chen:** Project administration, Funding acquisition. **Jin-Tao Liu:** Resources, Funding acquisition. **Min Xu:** Funding acquisition, Data curation.

# **Declaration of competing interest**

The authors declare that they have no known competing financial interests or personal relationships that could have appeared to influence the work reported in this paper.

### Acknowledgments

The Major projects support this research during the 14th Fiveyear Plan period under contract number 2021QNLM020001, the Major Scientific and Technological Projects of Shandong Energy Group under contract number SNKJ2022A06-R23, the National Natural Science Foundation of China under contract number 42374164, the Funds for Creative Research Groups of China under where  $M_{ij}(\omega)=C_{ij}\cos^2(\pi\gamma_{ij}/2)\left(\frac{i\omega}{\omega_0}\right)^{2\gamma_{ij}}$ . Next, we introduce an approximate expression  $(i\omega)^{2\gamma}\approx(i\omega)\sin(\pi\gamma)\nu^{2\gamma-1}k^{2\gamma-1}+\cos(\pi\gamma)\nu^{2\gamma}k^{2\gamma}$  to reduce the computational storage cost (Zhu et al., 2014). Note the phase velocity  $\nu$  associated with  $M_{13}$ ,  $M_{11}$ ,  $M_{33}$  can be expressed as  $\nu_{13}=\sqrt{C_{11}}=\nu_{\rm P}(1+2\varepsilon)^{1/2}$ ,  $\nu_{11}=\sqrt{C_{13}}=\nu_{\rm P}(1+2\delta)^{1/4}$ ,  $\nu_{33}=\sqrt{C_{33}}=\nu_{\rm P}$ , where  $\nu_{\rm P}$  is the P-wave velocity along the vertical axis of symmetry (Xiang et al., 2025). Then, we insert the approximate expression into the expression of  $M_{ij}(\omega)$ , resulting in

$$M_{ii} = i\omega \zeta_{ii} k^{2\gamma_{ij}-1} + \chi_{ii} k^{2\gamma_{ij}}, \tag{A.3}$$

where 
$$\zeta_{ij} = C_{ij}^{(\gamma_{ij}+1)} \cos^2(\pi \gamma_{ij}/2) \omega_0^{-2\gamma_{ij}} \cos(\pi \gamma_{ij})$$
,  $\chi_{ij} = C_{ij}^{(\gamma_{ij}+1/2)} \cos^2(\pi \gamma_{ij}/2) \omega_0^{-2\gamma_{ij}} \sin(\pi \gamma_{ij})$ .

By substituting Eq. (A.3) into Eq. (A.2) and transforming it to the time-space domain, we derive the pure viscoacoustic wave equation in the TTI attenuation medium:

$$\begin{split} \frac{\partial^{2}p}{\partial t^{2}} &= \left(\zeta_{11}\left(-\nabla^{2}\right)^{\gamma_{11}} + \chi_{11}\frac{\partial}{\partial t}\left(-\nabla^{2}\right)^{\gamma_{11}-1/2}\right) \left(\cos^{2}\phi \frac{\partial^{2}}{\partial x^{2}} + \sin^{2}\phi \frac{\partial^{2}}{\partial z^{2}} - \sin 2\phi \frac{\partial^{2}}{\partial x\partial z}\right) p \\ &+ \left(\zeta_{33}\left(-\nabla^{2}\right)^{\gamma_{33}} + \chi_{33}\frac{\partial}{\partial t}\left(-\nabla^{2}\right)^{\gamma_{33}-1/2}\right) \left(\sin^{2}\phi \frac{\partial^{2}}{\partial x^{2}} + \cos^{2}\phi \frac{\partial^{2}}{\partial z^{2}} + \sin 2\phi \frac{\partial^{2}}{\partial x\partial z}\right) p \\ &+ \left(a_{1}\left(-\nabla^{2}\right)^{\lambda_{33}\gamma_{33}} + b_{1}\frac{\partial}{\partial t}\left(-\nabla^{2}\right)^{\lambda_{33}\gamma_{33}-1/2} - a_{2}\left(-\nabla^{2}\right)^{\lambda_{11}\gamma_{11}} - b_{2}\frac{\partial}{\partial t}\left(-\nabla^{2}\right)^{\lambda_{11}\gamma_{11}-1/2}\right) \\ &\frac{1}{\frac{\partial^{2}}{\partial x^{2}} + \frac{\partial^{2}}{\partial z^{2}}} \begin{pmatrix} \sin^{2}\phi \cos^{2}\phi \left(k_{x}^{4} + k_{z}^{4}\right) \\ &+ \left(\cos^{4}\phi + \sin^{4}\phi - \sin^{2}2\phi\right) \frac{\partial^{4}}{\partial x^{2}\partial z^{2}} \\ &+ \sin 2\phi \left(\cos^{2}\phi - \sin^{2}\phi\right) \frac{\partial^{4}}{\partial x^{3}\partial z} \\ &+ \sin 2\phi \left(\sin^{2}\phi - \cos^{2}\phi\right) \frac{\partial^{4}}{\partial x^{3}\partial z} \end{pmatrix} p + f. \end{split}$$

Since the mixed-domain fractional Laplacian operator of these equations varies with the quality factor of the space, Eq. (A.4) cannot be solved directly by the traditional Fourier pseudo-

$$\nabla^{2\gamma_{ij}(x)} \approx F^{-1} \left( 1 + 2 \left( \ln(k) \gamma_{ij}(x) + \left( \ln(k) \gamma_{ij}(x) \right)^2 \right) \right). \tag{A.5}$$

Substituting Eq. (A.5) into Eq. (A.4), the pure viscoacoustic TTI wave Eq. (A.2) using the HFDPS strategy can be rewritten as

$$\begin{split} &\frac{\partial^{2}p}{\partial t^{2}} = \left(\cos^{2}\phi \frac{\partial^{2}}{\partial x^{2}} - \sin 2\phi \frac{\partial^{2}}{\partial x \partial z} + \sin^{2}\phi \frac{\partial^{2}}{\partial z^{2}}\right) \begin{pmatrix} \zeta_{11} \left(p + 2\gamma_{11}(x)L_{1} + 2\gamma_{11}^{2}(x)L_{2}\right) \\ + \chi_{11} \left(L_{3} + 2L_{4}\gamma_{11}(x) + 2\gamma_{11}^{2}(x)L_{5}\right) \end{pmatrix} \\ &+ \left(\sin^{2}\phi \frac{\partial^{2}}{\partial x^{2}} + \sin 2\phi \frac{\partial^{2}}{\partial x \partial z} + \cos^{2}\phi \frac{\partial^{2}}{\partial z^{2}}\right) \begin{pmatrix} \zeta_{33} \left(p + 2\gamma_{33}(x)L_{1} + 2\gamma_{33}^{2}(x)L_{2}\right) \\ + \chi_{33} \left(L_{3} + 2L_{4}\gamma_{33}(x) + 2\gamma_{33}^{2}(x)L_{5}\right) \end{pmatrix} \\ &- \begin{pmatrix} \sin^{2}\phi \cos^{2}\phi \left(k_{x}^{4} + k_{z}^{4}\right) \\ + \left(\cos^{4}\phi + \sin^{4}\phi - \sin^{2}2\phi\right)k_{x}^{2}k_{z}^{2} \\ + \sin 2\phi \left(\cos^{2}\phi - \sin^{2}\phi\right)k_{x}^{3}k_{z} \\ + \sin 2\phi \left(\sin^{2}\phi - \cos^{2}\phi\right)k_{x}k_{z}^{3} \end{pmatrix} \begin{pmatrix} a_{1}\left(L_{6} + 2L_{7}\lambda_{33}\gamma_{33}(x) + 2(\lambda_{33}\gamma_{33}(x))^{2}L_{8}\right) \\ + b_{1}\left(L_{9} + 2L_{10}\lambda_{33}\gamma_{33}(x) + 2(\lambda_{11}\gamma_{11}(x))^{2}L_{8}\right) \\ - a_{2}\left(L_{6} + 2L_{7}\lambda_{11}\gamma_{11}(x) + 2(\lambda_{11}\gamma_{11}(x))^{2}L_{8}\right) \\ - b_{2}\left(L_{9} + 2L_{10}\lambda_{11}\gamma_{11}(x) + 2L_{11}(\lambda_{11}\gamma_{11}(x))^{2}\right) \end{pmatrix} + f, \end{split}$$

spectral (FPS) and finite difference (FD) methods. Subsequently, Zhang et al. (2020) used the second-order TSE  $k^{2\gamma_{ij}(x)} \approx 1 + 2(\ln(k)\gamma_{ij}(x) + (\ln(k)\gamma_{ij}(x))^2)$  to simplify these equations, which in the space domain would be expressed as

where f is the source-time function, and  $\zeta_{ij}$ ,  $\chi_{ij}$ ,  $a_i$ ,  $b_i$  can be expressed as

$$\begin{split} \zeta_{ij} &= C_{ij}^{\left(\gamma_{ij}+1\right)} \cos^2\!\left(\pi\gamma_{ij}\middle/2\right) \omega_0^{-2\gamma_{ij}} \cos\!\left(\pi\gamma_{ij}\right), \;\; \chi_{ij} &= C_{ij}^{\left(\gamma_{ij}+1/2\right)} \cos^2\!\left(\pi\gamma_{ij}\middle/2\right) \omega_0^{-2\gamma_{ij}} \sin\!\left(\pi\gamma_{ij}\right), \\ a_1 &= (\zeta_{13})^2\!\left(\sqrt{\zeta_{11}\zeta_{33}}\right)^{-1}, \;\; b_1 &= (\chi_{13})^2\!\left(\sqrt{\chi_{11}\chi_{33}}\right)^{-1}, \;\; a_2 &= \sqrt{\zeta_{11}\zeta_{33}}, \;\; b_2 &= \sqrt{\chi_{11}\chi_{33}}. \end{split}$$

Subsequently, by substituting Eq. (2) into Eq. (A.6), the pure viscoacoustic TTI wave equation can be rewritten as

$$\begin{split} \frac{\partial^{2}p}{\partial t^{2}} &= \Psi_{11} \Big( \zeta_{11} \Big( p + 2\gamma_{11}(x) L_{1} + 2\gamma_{11}^{2}(x) L_{2} \Big) \\ &+ \chi_{11} \Big( L_{3} + 2L_{4}\gamma_{11}(x) + 2\gamma_{11}^{2}(x) L_{5} \Big) \Big) \\ &+ \Psi_{33} \Big( \zeta_{33} \Big( p + 2\gamma_{33}(x) L_{1} + 2\gamma_{33}^{2}(x) L_{2} \Big) \\ &+ \chi_{33} \Big( L_{3} + 2L_{4}\gamma_{33}(x) + 2\gamma_{33}^{2}(x) L_{5} \Big) \Big) \\ &- \Psi_{13} \begin{pmatrix} a_{1} \Big( L_{6} + 2L_{7}\lambda_{33}\gamma_{33}(x) + 2(\lambda_{33}\gamma_{33}(x))^{2} L_{8} \Big) \\ &+ b_{1} \Big( L_{9} + 2L_{10}\lambda_{33}\gamma_{33}(x) + 2L_{11}(\lambda_{33}\gamma_{33}(x))^{2} \Big) \\ &- a_{2} \Big( L_{6} + 2L_{7}\lambda_{11}\gamma_{11}(x) + 2(\lambda_{11}\gamma_{11}(x))^{2} L_{8} \Big) \\ &- b_{2} \Big( L_{9} + 2L_{10}\lambda_{11}\gamma_{11}(x) + 2L_{11}(\lambda_{11}\gamma_{11}(x))^{2} \Big) \end{pmatrix} \end{split}$$
 (A.7)

#### APPENDIX B

Derivation of the anisotropic attenuation-compensated extrapolation operator.

Based on the stable term  $\Upsilon(1-\tau\omega)\omega$  proposed by Mu et al. (2023). We extend it to attenuation anisotropic media. The corrected analytic expression of attenuation compensation in attenuation anisotropic media can expressed as

$$P(t + \Delta t, \omega) = P(t, \omega) \exp\left[\Upsilon_{ij}(1 - \tau\omega)\omega\Delta t\omega_0^{\gamma_{ij}}\omega^{1 - \gamma_{ij}} \tan\left(\pi\gamma_{ij} / 2\right)\right],$$
(B.1)

where  $\tau$  is the stability factor.  $\Upsilon_{ij}$  is a constant that is associated with  $\tau$  and can be determined accordingly using the following relational formula:

where  $\tau=1/(2\omega_{\tau})$ .  $\omega_{\tau}=2\pi(f_{\tau}+f_{s})$ , which is slightly higher than the peak angular frequency of the source wavelet  $2\pi f_{s}$ .  $f_{\tau}$  denotes the increment of frequency. Through numerous numerical experiments, Mu et al. (2023) concluded that the  $f_{\tau}$   $\in$  (5, 20). Subsequently, by substituting Eq. (B.1) into Eq. (10), we can obtain the analytic expression of the stability anisotropic attenuation-compensation operator in attenuation anisotropic media:

$$\begin{split} &P(t+\Delta t,\omega) = P(t,\omega) \text{exp} \Big[ \Upsilon_{ij} (1-\tau\omega) \omega \Delta t \omega_0^{\gamma} \omega_m^{1-\gamma} \, \tan(\pi\gamma/2) \Big] \\ &\times \text{exp} \Big[ -i \Delta t \omega_0^{\gamma} \omega^{1-\gamma} \Big]. \end{split} \tag{B.3}$$

Combining the formula of  $P(x + \Delta x, \omega) = P(x, \omega)e^{ik_{ij}(\omega)\sqrt{C_{ij}}\Delta t}$ , the approximate dispersion relation of Eq. (B.3) can be written as

$$k_{ij}(\omega) = \frac{\omega_0^{\gamma_{ij}} \omega^{1-\gamma_{ij}}}{\sqrt{C_{ij}}} \left( i \Upsilon_{ij} (1 - \tau \omega) \omega \tan(\pi \gamma / 2) + 1 \right), \tag{B.4}$$

where  $k_{ij}(\omega)$  denote the approximate dispersion relation of CQ theory in attenuation anisotropic media. By using the relational expression  $V_{ij}^2(\omega) = \omega^2/k_{ij}^2(\omega)$  and some mathematical derivation, we obtain the following expression:

$$\tilde{M}_{ij}(\omega) = V_{ij}^{2}(\omega) = \frac{C_{ij} \left(\omega_{0}^{-\gamma_{ij}} \omega^{\gamma_{ij}}\right)^{2}}{\left(1 + i \Upsilon_{ij} (1 - \tau \omega) \omega \tan\left(\pi \gamma_{ij} / 2\right)\right)^{2}}.$$
(B.5)

To simplify the analytic relation, we ignored the  $\Upsilon_{ij}^2$  term to the right of Eq. (B.5) due to the value of  $\Upsilon_{ij}$  is small. Then, we can obtain the attenuation-compensated complex velocity formula as follows:

$$\tilde{M}_{ij}(\omega) \approx C_{ij} \left( \omega_0^{-\gamma_{ij}} \omega^{\gamma_{ij}} \right)^2 \left( 1 - 2i \Upsilon_{ij} (1 - \tau \omega) \omega \tan \left( \pi \gamma_{ij} / 2 \right) \right). \tag{B.6}$$

Subsequently, inserting Eq. (B.6) into Eq. (5) and replacing  $M_{ij}$  with  $\tilde{M}_{ij}$ . We can obtain the high-efficiency attenuation-compensated RTM operator in TTI media expressed as

$$\omega^{2} \approx \frac{\tilde{M}_{11}}{k_{x}^{2} + k_{z}^{2}} \left( \sin^{2} \phi k_{x}^{4} + \cos^{2} \phi k_{x}^{4} + k_{x}^{2} k_{z}^{2} - \sin 2 \phi \left( k_{x}^{3} k_{z} + k_{x} k_{z}^{3} \right) \right)$$

$$+ \frac{\tilde{M}_{33}}{k_{x}^{2} + k_{z}^{2}} \left( \sin^{2} \phi k_{x}^{4} + \cos^{2} \phi k_{z}^{4} + k_{x}^{2} k_{z}^{2} + \sin 2 \phi \left( k_{x}^{3} k_{z} + k_{x} k_{z}^{3} \right) \right)$$

$$+ \frac{\tilde{M}_{13}^{2} \left( \sqrt{\tilde{M}_{11} \tilde{M}_{33}} \right)^{-1} - \sqrt{\tilde{M}_{11} \tilde{M}_{33}}}{k_{x}^{2} + k_{z}^{2}} \begin{pmatrix} \sin^{2} \phi \cos^{2} \phi \left( k_{x}^{4} + k_{z}^{4} \right) \\ + \left( \cos^{4} \phi + \sin^{4} \phi - \sin^{2} 2 \phi \right) k_{x}^{2} k_{z}^{2} \\ + \sin 2 \phi \left( \cos^{2} \phi - \sin^{2} \phi \right) k_{x}^{3} k_{z} \\ + \sin 2 \phi \left( \sin^{2} \phi - \cos^{2} \phi \right) k_{x} k_{z}^{3} \end{pmatrix}.$$

$$(B.7)$$

$$\begin{split} &\exp\left[\Upsilon_{ij}(1-\tau\omega)\omega\Delta t\omega_{0}^{\gamma_{ij}}\omega^{1-\gamma_{ij}}\,\tan\!\left(\!\frac{\pi\gamma_{ij}}{2}\!\right)\right]\Big|_{\omega=\omega_{\max}} \\ &=\exp\!\left[\Delta t\omega_{0}^{\gamma_{ij}}\omega^{1-\gamma_{ij}}\,\tan\!\left(\!\frac{\pi\gamma_{ij}}{2}\!\right)\right]\Big|_{\omega=\omega_{\max}}, \end{split} \tag{B.2}$$

Similar to the derivation of Eq. (A.2), using approximate relational expressions to obtain the efficient and stable attenuation-compensated extrapolation equation based on the algebraic method in the attenuation TTI media written as:

$$\frac{\partial^{2} p}{\partial t^{2}} = \frac{1}{\frac{\partial^{2}}{\partial x^{2}} + \frac{\partial^{2}}{\partial z^{2}}} \begin{pmatrix}
\widehat{\Psi}_{11} \left( \zeta_{11}^{1} \left( -\nabla^{2} \right)^{\gamma_{11}} + \zeta_{11}^{2} \frac{\partial}{\partial t} \left( -\nabla^{2} \right)^{\gamma_{11}} + \zeta_{11}^{3} \frac{\partial}{\partial t} \left( -\nabla^{2} \right)^{\gamma_{11}+1} \right) \\
+ \widehat{\Psi}_{33} \left( \zeta_{33}^{1} \left( -\nabla^{2} \right)^{\gamma_{33}} + \zeta_{33}^{2} \frac{\partial}{\partial t} \left( -\nabla^{2} \right)^{\gamma_{33}} + \zeta_{33}^{3} \frac{\partial}{\partial t} \left( -\nabla^{2} \right)^{\gamma_{33}+1} \right) \\
- \left( \Psi_{1} \left( -\nabla^{2} \right)^{\mu_{33}\gamma_{33}} - \Psi_{2} \frac{\partial}{\partial t} \left( -\nabla^{2} \right)^{\mu_{33}\gamma_{33}-\frac{1}{2}} - \Psi_{3} \frac{\partial}{\partial t} \left( -\nabla^{2} \right)^{\frac{3}{2}\mu_{33}\gamma_{33}+\frac{\tau}{2}-1} \right) \\
+ \Psi_{13} \left( \xi_{1} \left( -\nabla^{2} \right)^{\mu_{11}\gamma_{11}} - \xi_{2} \frac{\partial}{\partial t} \left( -\nabla^{2} \right)^{\mu_{11}\gamma_{11}-\frac{1}{2}} - \xi_{3} \frac{\partial}{\partial t} \left( -\nabla^{2} \right)^{\frac{3}{2}\mu_{11}\gamma_{11}+\frac{\tau}{2}-1} \right)
\end{pmatrix}$$
(B.8)

where  $\psi_i = (\zeta_{13}^i)^2 (\sqrt{\zeta_{11}^i \zeta_{33}^i})^{-1}$ ,  $\xi_i = \sqrt{\zeta_{11}^i \zeta_{33}^i}$ 

## APPENDIX C

Derivation of traditional Q-compensated pure viscoacoustic TTI

wave equation.

According to Eq. (B.8), the conventional stable attenuation-compensated pure viscoacoustic TTI wave equation can be obtained as follows:

$$\begin{split} &\frac{\partial^{2}p}{\partial t^{2}} = \Psi_{11} \left( \zeta_{11}^{1} \left( -\nabla^{2} \right)^{\gamma_{11}} + \zeta_{11}^{2} \frac{\partial}{\partial t} \left( -\nabla^{2} \right)^{\gamma_{11}} \right. \\ &+ \left. \zeta_{11}^{3} \frac{\partial}{\partial t} \left( -\nabla^{2} \right)^{\gamma_{11}+1} \right) p + \Psi_{33} \left( \zeta_{33}^{1} \left( -\nabla^{2} \right)^{\gamma_{33}} \right. \\ &+ \left. \zeta_{33}^{2} \frac{\partial}{\partial t} \left( -\nabla^{2} \right)^{\gamma_{33}} + \zeta_{33}^{3} \frac{\partial}{\partial t} \left( -\nabla^{2} \right)^{\gamma_{33}+1} \right) p \\ &+ \frac{\Psi_{13}}{\frac{\partial^{2}}{\partial x^{2}} + \frac{\partial^{2}}{\partial z^{2}}} \left( \psi_{1} \left( -\nabla^{2} \right)^{\mu_{33}\gamma_{33}} + \psi_{2} \frac{\partial}{\partial t} \left( -\nabla^{2} \right)^{\mu_{33}\gamma_{33}} + \psi_{3} \frac{\partial}{\partial t} \left( -\nabla^{2} \right)^{\mu_{33}\gamma_{33}+1} \right. \\ &+ \left. \left. \left. \left( \xi_{1} \left( -\nabla^{2} \right)^{\mu_{11}\gamma_{11}} + \xi_{2} \frac{\partial}{\partial t} \left( -\nabla^{2} \right)^{\mu_{11}\gamma_{11}} + \xi_{3} \frac{\partial}{\partial t} \left( -\nabla^{2} \right)^{\mu_{11}\gamma_{11}+1} \right) \right. \right) p + f. \end{split}$$

To improve readability and facilitate understanding, we define the following conventions:

$$\begin{split} H_{ij} &= \begin{pmatrix} \zeta_{ij}^1 \Big( P + 2\gamma_{ij}(x) L_1' + 2\gamma_{ij}^2(x) L_2' \Big) - \zeta_{ij}^2 \Big( L_3' + 2\gamma_{ij}(x) L_4' + 2\gamma_{ij}^2(x) L_5' \Big) \\ - \zeta_{ij}^3 \Big( L_6' + 2\gamma_{ij}(x) L_1' + 2\gamma_{ij}^2(x) L_1' \Big) + \zeta_{ij}^2 \Big( L_{12}' + 2\gamma_{ij}(x) L_{13}' + 2\gamma_{ij}^2(x) L_{14}' \Big) \\ + \zeta_{ij}^3 \Big( L_{15}' + 2\gamma_{ij}(x) L_{16}' + 2\gamma_{ij}^2(x) L_{17}' \Big) \end{pmatrix}, \\ H''' &= \begin{pmatrix} \zeta_{ij}^1 \Big( L_9' + 2\gamma_{ij}(x) L_{10}' + 2\gamma_{ij}^2(x) L_{11}' \Big) + \zeta_{ij}^2 \Big( L_{12}' + 2\gamma_{ij}(x) L_{13}' + 2\gamma_{ij}^2(x) L_{14}' \Big) \\ + \zeta_{ij}^3 \Big( L_{15}' + 2\gamma_{ij}(x) L_{16}' + 2\gamma_{ij}^2(x) L_{17}' \Big) \end{pmatrix}, \\ H''' &= \begin{pmatrix} \psi_1 \Big( P + 2_2 \lambda_{33} \gamma_{33}(x) L_1' + 2(\lambda_{33} \gamma_{33}(x))^2 L_2' \Big) + \psi_2 \Big( L_3' + 2\lambda_{33} \gamma_{33}(x) L_4' + 2(\lambda_{33} \gamma_{33}(x))^2 L_5' \Big) \\ + \psi_3 \Big( L_6' + 2\lambda_{33} \gamma_{33}(x) L_7' + 2(\lambda_{33} \gamma_{33}(x))^2 L_8' \Big) - \xi_1 \Big( P + 2\lambda_{11} \gamma_{11}(x) L_1' + 2(\lambda_{11} \gamma_{11}(x))^2 L_2' \Big) \\ - \xi_2 \Big( L_3' + 2\lambda_{11} \gamma_{11}(x) L_4' + 2(\lambda_{11} \gamma_{11}(x))^2 L_5' \Big) - \xi_3 \Big( L_6' + 2\lambda_{11} \gamma_{11}(x) L_7' + 2(\lambda_{11} \gamma_{11}(x))^2 L_8' \Big) \end{pmatrix}, \\ H'''' &= \begin{pmatrix} \psi_1 \Big( L_9' + 2_2 \lambda_{33} \gamma_{33}(x) L_{10}' + 2(\lambda_{33} \gamma_{33}(x))^2 L_{11}' \Big) - \psi_2 \Big( L_{12}' + 2\lambda_{33} \gamma_{33}(x) L_{13}' + 2(\lambda_{33} \gamma_{33}(x))^2 L_{14}' \Big) \\ - \psi_3 \Big( L_{15}' + 2\lambda_{33} \gamma_{33}(x) L_{16}' + 2(\lambda_{33} \gamma_{33}(x))^2 L_{17}' \Big) - \xi_1 \Big( L_9' + 2\lambda_{11} \gamma_{11}(x) L_{10}' + 2(\lambda_{11} \gamma_{11}(x))^2 L_{11}' \Big) \\ + \xi_2 \Big( L_{12}' + 2\lambda_{11} \gamma_{11}(x) L_{13}' + 2(\lambda_{11} \gamma_{11}(x))^2 L_{14}' \Big) + \xi_3 \Big( L_{15}' + 2\lambda_{11} \gamma_{11}(x) L_{16}' + 2(\lambda_{11} \gamma_{11}(x))^2 L_{17}' \Big) \end{pmatrix}$$

$$\begin{split} &\text{where } L_1' = \mathcal{F}^{-1}(\ln(k)\mathcal{F}(p)), L_2' = \mathcal{F}^{-1}(\ln(k)^2\mathcal{F}(p)), L_3' = \mathcal{F}^{-1} \\ & \left(\mathcal{F}\left(\frac{\partial p}{\partial t}\right)\right), \ L_4' = \mathcal{F}^{-1}\left(\mathcal{F}\left(\frac{\partial p}{\partial t}\right)\ln(k)\right), \ L_5' = \mathcal{F}^{-1}\left(\mathcal{F}\left(\frac{\partial p}{\partial t}\right)\ln(k)^2\right), \\ & L_6' = \mathcal{F}^{-1}\left(k\mathcal{F}\left(\frac{\partial p}{\partial t}\right)\right), \ L_7' = \mathcal{F}^{-1}\left(k\mathcal{F}\left(\frac{\partial p}{\partial t}\right)\ln(k)\right), \ L_8' = \mathcal{F}^{-1} \\ & \left(k\mathcal{F}\left(\frac{\partial p}{\partial t}\right)\ln(k)^2\right), \ L_9' = \mathcal{F}^{-1}((k_x^2+k_z^2)^{-1}\mathcal{F}(p)), \ L_{10}' = \mathcal{F}^{-1} \\ & \left((k_x^2+k_z^2)^{-1}\mathcal{F}(p)\ln(k)\right), \ L_{11}' = \mathcal{F}^{-1}((k_x^2+k_z^2)^{-1}\mathcal{F}(p)\ln(k)^2), \\ & L_{12}' = \mathcal{F}^{-1}\left((k_x^2+k_z^2)^{-1}\mathcal{F}\left(\frac{\partial p}{\partial t}\right)\right), \ L_{13}' = \mathcal{F}^{-1}\left((k_x^2+k_z^2)^{-1}\mathcal{F}\left(\frac{\partial p}{\partial t}\right)\ln(k)^2\right), \ L_{15}' = \mathcal{F}^{-1} \\ & \left(k(k_x^2+k_z^2)^{-1}\mathcal{F}\left(\frac{\partial p}{\partial t}\right)\right), \ L_{16}' = \mathcal{F}^{-1}\left(k(k_x^2+k_z^2)^{-1}\mathcal{F}\left(\frac{\partial p}{\partial t}\right)\ln(k)\right), \\ & L_{17}' = \mathcal{F}^{-1}\left(k(k_x^2+k_z^2)^{-1}\mathcal{F}\left(\frac{\partial p}{\partial t}\right)\ln(k)^2\right). \end{split}$$

Subsequently, similar to the derivation of Eq. (7), Eq. (C.1) can be

the new expression as follows:

$$\omega^{2} \approx M_{11}k_{x}^{2} + M_{33}k_{z}^{2} + \frac{k_{x}^{2}k_{z}^{2} \left(M_{13}^{2} \left(\sqrt{M_{11}M_{33}}\right)^{-1} - \sqrt{M_{11}M_{33}}\right) \left(k_{x}^{2} + k_{z}^{2}\right)}{\left(k_{x}^{2} + k_{z}^{2}\right) \left(k_{x}^{2} + k_{z}^{2}\right)}.$$
 (D.1)

Next, the coordinate rotation relations  $\widehat{k}_X = \cos\phi k_X - \sin\phi$ ,  $\widehat{k}_Z = \sin\phi k_X + \cos\phi k_Z$  are used to transform Eq. (D.1) from VTI media to TTI media. Note that  $\phi$  represent the dip angle of the symmetry axis. Replacing  $k_X, k_Z$  in Eq. (C.1) with  $\widehat{k}_X, \widehat{k}_Z$ , we can obtain the TTI approximation dispersion relation

$$\left(k_{x}^{2}+k_{z}^{2}\right) \begin{pmatrix} M_{13}^{2}\left(\sqrt{M_{11}M_{33}}\right)^{-1} \\ -\sqrt{M_{11}M_{33}} \end{pmatrix}^{-1} \begin{pmatrix} \sin^{2}\phi\cos^{2}\phi\left(k_{x}^{4}+k_{z}^{4}\right) \\ +\left(\cos^{4}\phi+\sin^{4}\phi-\sin^{2}2\phi\right)k_{x}^{2}k_{z}^{2} \\ +\sin2\phi\left(\cos^{2}\phi-\sin^{2}\phi\right)k_{x}^{3}k_{z} \\ +\sin2\phi\left(\sin^{2}\phi-\cos^{2}\phi\right)k_{x}k_{z}^{3} \end{pmatrix} \\ \omega^{2} \approx M_{11}\Gamma_{11} + M_{33}\Gamma_{33} + \frac{\left(k_{x}^{2}+k_{z}^{2}\right)^{2}}{\left(k_{x}^{2}+k_{z}^{2}\right)^{2}}.$$
 (D.2)

reformulated as

$$\frac{\partial^2 p}{\partial t^2} = (\Psi_{11} H_{11} + \Psi_{33} H_{33} + \Psi_{13} H^{"}) P + f, \tag{C.2}$$

Analyzing the above Eq. (C.2), the traditional stable attenuation compensation pure viscoacoustic wave equation contains 17 FFTs, resulting in a significant computational cost. This presents challenges for practical applications of the field data and three-dimensional data in anisotropic attenuation media.

#### APPENDIX D

Derivation of HE-HFDPS strategy based on the asymptotic approximation method.

To use the asymptotic approximation, we multiply the correction term of Eq. (1) by the expression  $(\frac{k_x^2+k_z^2}{k_x^2+k_z^2})$  and then we can obtain

To improve readability and facilitate understanding, we define the following conventions  $\Gamma_{11} = \sin^2 \phi k_z^2 + \cos^2 \phi k_x^2 - \sin 2 \phi k_x k_z$ ,  $\Gamma_{33} = \sin^2 \phi k_x^2 + \cos^2 \phi k_z^2 + \sin 2 \phi k_x k_z$ .

Note that we assume the propagation direction  $\mathbf{n}=(n_x,n_z)=(\sin\theta,\cos\theta)$  for the TTI media.  $\mathbf{n}$  represent the phase direction of wave propagation which is a unit vector. In addition, the relation between frequency and wavenumber in TTI media are  $\sin\theta=k_x/k$ ,  $\cos\theta=k_z/k$  and thus we can obtain the relation between  $\mathbf{n}$  and  $\mathbf{k}$  as

$$\mathbf{n} = (n_x, n_z) = (\sin \theta, \cos \theta) = \left(\frac{k_x}{k}, \frac{k_z}{k}\right) = \frac{\mathbf{k}}{|\mathbf{k}|}.$$
 (D.3)

Substituting Eq. (D.3) into Eq. (D.2), Eq. (D.2) can be rewritten as

$$\left(k_{x}^{2}+k_{z}^{2}\right) \begin{pmatrix} M_{13}^{2}\left(\sqrt{M_{11}M_{33}}\right)^{-1} \\ -\sqrt{M_{11}M_{33}} \end{pmatrix}^{-1} \begin{pmatrix} \sin^{2}\phi\cos^{2}\phi\left(n_{x}^{4}+n_{z}^{4}\right) \\ +\left(\cos^{4}\phi+\sin^{4}\phi-\sin^{2}2\phi\right)n_{x}^{2}n_{z}^{2} \\ +\sin 2\phi\left(\cos^{2}\phi-\sin^{2}\phi\right)n_{x}^{3}n_{z} \\ +\sin 2\phi\left(\sin^{2}\phi-\cos^{2}\phi\right)n_{z}^{3}n_{x} \end{pmatrix}$$

$$\omega = M_{11}\Gamma_{11} + M_{33}\Gamma_{33} + \frac{\left(n_{x}^{2}+n_{z}^{2}\right)^{2}}{\left(n_{x}^{2}+n_{z}^{2}\right)^{2}} .$$
 (D.4)

Based on the asymptotic approximation ( $\mathbf{n} = \mathbf{k}/|\mathbf{k}| = \nabla P/|\nabla P|$ ) proposed by Xu and Zhou (2014), the  $\mathbf{n}$ ,  $n_X$  and  $n_Z$  can be expressed as

$$\mathbf{n} = \left(\frac{\partial P}{\partial x}\mathbf{e}_{x} + \frac{\partial P}{\partial z}\mathbf{e}_{z}\right) / \left|\frac{\partial P}{\partial x}\mathbf{e}_{x} + \frac{\partial P}{\partial z}\mathbf{e}_{z}\right|,$$

$$n_{x} = \frac{\partial P}{\partial x} / \sqrt{\left(\frac{\partial P}{\partial x}\right)^{2} + \left(\frac{\partial P}{\partial z}\right)^{2}}, n_{z} = \frac{\partial P}{\partial z} / \sqrt{\left(\frac{\partial P}{\partial x}\right)^{2} + \left(\frac{\partial P}{\partial z}\right)^{2}},$$
(D.5)

where P represents the pressure wavefield. Subsequently, by inserting Eq. (D.5) into Eq. (D.4), then Eq. (D.4) can be rewritten as

$$\omega^{2} \approx M_{11}\Gamma_{11} + M_{33}\Gamma_{33} + T_{s} \begin{pmatrix} M_{13}^{2} \left(\sqrt{M_{11}M_{33}}\right)^{-1} \\ -\sqrt{M_{11}M_{33}} \end{pmatrix} \left(k_{x}^{2} + k_{z}^{2}\right).$$
(D.6)

Note that  $T_s$  term of the right-hand side in Eq. (C.6) is defined as a scalar operator, which can be defined as follows:

$$\begin{split} \frac{\partial^{2}p}{\partial t^{2}} &= \varPsi_{11} \Big( \zeta_{11} \Big( P + 2\gamma_{11}(x)L_{1} + 2\gamma_{11}^{2}(x)L_{2} \Big) + \chi_{11} \Big( L_{3} \\ &+ 2L_{4}\gamma_{11}(x) + 2\gamma_{11}^{2}(x)L_{5} \Big) \Big) + \varPsi_{33} \Big( \zeta_{33} \Big( P + 2\gamma_{33}(x)L_{1} \\ &+ 2\gamma_{33}^{2}(x)L_{2} \Big) + \chi_{33} \Big( L_{3} + 2L_{4}\gamma_{33}(x) + 2\gamma_{33}^{2}(x)L_{5} \Big) \Big) \\ &+ T_{s} \Bigg( \frac{\partial^{2}}{\partial x^{2}} + \frac{\partial^{2}}{\partial z^{2}} \Bigg) \\ &\times \begin{pmatrix} a_{1} \Big( P + 2L_{1}\lambda_{33}\gamma_{33}(x) + 2(\lambda_{33}\gamma_{33}(x))^{2}L_{2} \Big) \\ &+ b_{1} \Big( L_{3} + 2L_{4}\lambda_{33}\gamma_{33}(x) + 2L_{5}(\lambda_{33}\gamma_{33}(x))^{2} \Big) \\ &- a_{2} \Big( P + 2L_{1}\lambda_{11}\gamma_{11}(x) + 2(\lambda_{11}\gamma_{11}(x))^{2}L_{2} \Big) \\ &- b_{2} \Big( L_{3} + 2L_{4}\lambda_{11}\gamma_{11}(x) + 2L_{5}(\lambda_{11}\gamma_{11}(x))^{2} \Big) \end{pmatrix} + f. \end{split}$$
 (D.9)

From the above Eq. (D.10), we will find that the proposed HE-HFDPS strategy based on the asymptotic approximation method only retains  $L_1-L_5$ , reducing the number of FFT calculations from 11 to 5 per time step. In addition, it only contains 2-order spatial

$$T_{s} = \frac{\left(\sin^{2s}\phi\cos^{2}\phi\left(\left(\frac{\partial P}{\partial x}\right)^{4} + \left(\frac{\partial P}{\partial z}\right)^{4}\right) + \left(\cos^{4}\phi + \sin^{4}\phi - \sin^{2}2\phi\right)\left(\frac{\partial P}{\partial x}\frac{\partial P}{\partial z}\right)^{2}}{+\sin 2\phi\left(\cos^{2}\phi - \sin^{2}\phi\right)\left(\frac{\partial P}{\partial x}\right)^{3}\frac{\partial P}{\partial z} + \sin 2\phi\left(\sin^{2}\phi - \cos^{2}\phi\right)\left(\frac{\partial P}{\partial z}\right)^{3}\frac{\partial P}{\partial x}}\right)}{\left(\left(\frac{\partial P}{\partial x}\right)^{2} + \left(\frac{\partial P}{\partial z}\right)^{2}\right)^{2}}.$$
(D.7)

Similar to the derivation process of Eq. (6), the new efficient pure viscoacoustic TTI wave equation can be obtained as partial derivatives, further improving the computational efficiency. Subsequently, inserting Eq. (B.7) into Eq. (D.7) and replacing  $M_{ij}$  with  $\tilde{M}_{ij}$ . Then, by some mathematical derivation, we can obtain the efficient and stable attenuation-compensated extrapolation equa-

$$\frac{\partial^{2} p}{\partial t^{2}} = \Psi_{11} \left( \zeta_{11} \left( -\nabla^{2} \right)^{\gamma_{11}} + \chi_{11} \frac{\partial}{\partial t} \left( -\nabla^{2} \right)^{\gamma_{11}} \frac{1}{2} \right) P + \Psi_{33} \left( \zeta_{33} \left( -\nabla^{2} \right)^{\gamma_{33}} + \chi_{33} \frac{\partial}{\partial t} \left( -\nabla^{2} \right)^{\gamma_{33}} \frac{1}{2} \right) P \\
+ T_{5} \left( \frac{\partial^{2}}{\partial x^{2}} + \frac{\partial^{2}}{\partial z^{2}} \right) \begin{pmatrix} a_{1} \left( -\nabla^{2} \right)^{\mu_{33}\gamma_{33}} + b_{1} \frac{\partial}{\partial t} \left( -\nabla^{2} \right)^{\mu_{33}\gamma_{33}} \frac{1}{2} \\
-a_{2} \left( -\nabla^{2} \right)^{\mu_{11}\gamma_{11}} - b_{2} \frac{\partial}{\partial t} \left( -\nabla^{2} \right)^{\mu_{11}\gamma_{11}} \frac{1}{2} \end{pmatrix} P + f. \tag{D.8}$$

Subsequently, we can simulate the pure viscoacoustic TTI wave equation using the HE-HFDPS strategy based on the asymptotic approximation method as follows:

tion using the HE-HFDPS strategy based on the asymptotic approximation as follows:

$$\frac{\partial^2 p}{\partial t^2} = \left( \Psi_{11} H_{11} + \Psi_{33} H_{33} + T_s \left( \frac{\partial^2}{\partial x^2} + \frac{\partial^2}{\partial z^2} \right) H^{"} \right) P + f.$$
(D.10)

Compared to the traditional HFDPS strategy Eq. (C.2), which requires 17 FFTs ( $L'_1-L'_{17}$ ) per time step, the proposed HE-HFDPS

numerical solution strategy only retains 8 FFTs  $(L'_1-L'_8)$ , reducing the number of FFTs from 17 to 8 per time step. That demonstrates that the asymptotic approximation method has significant potential for improved computational efficiency in *Q*-compensated RTM.

#### References

- Alkhalifah, T., 1998. Acoustic approximations for processing in transversely isotropic media. Geophysics 63 (2), 623–631. https://doi.org/10.1190/1.1444361.
- Aki, K., Richards, P.G., 2002. Quantitative Seismology, second ed. University Science Books, Herndon, VA, pp. 37–59.
- Carcione, J.M., Kosloff, D., Kosloff, R., 1988. Viscoacoustic wave propagation simulation in the earth. Geophysics 53 (6), 769–777. https://doi.org/10.1190/1.1442512.
- Carcione, J.M., 1992. Anisotropic Q and velocity dispersion of finely layered media1.

  Geophys. Prospect. 40 (7), 761–783. https://doi.org/10.1111/j.1365-2478.1992.tb00551.x.
- Carcione, J.M., Cavallini, F., Mainardi, F., 2002. Time-domain seismic modeling of constant Q-wave propagation using fractional derivatives. Pure Appl. Geophys. 159, 1719—1736. https://doi.org/10.1007/s00024-002-8705-z.
- Carter, A.J., Kendall, J.M., 2006. Attenuation anisotropy and the relative frequency content of split shear waves. Geophys. J. Int. 165 (3), 865–874. https://doi.org/ 10.1111/j.1365-246X.2006.02929.x.
- Carcione, J.M., 2007. Wave fields in real media: wave propagation in anisotropic, anelastic. Porous and Electromagnetic Media. Elsevier, Amsterdam.
- Cerjan, C., Kosloff, D., Kosloff, R., et al., 1985. A non-reflecting boundary condition for discrete acoustic and elastic wave equations. Geophysics 50 (4), 705–708. https://doi.org/10.1190/1.1441945.
- Chen, H.M., Zhou, H., Li, Q.Q., et al., 2016. Two efficient modeling schemes for fractional Laplacian viscoacoustic wave equation. Geophysics 81 (5), T233-T249. https://doi.org/10.1190/geo2015-0660.1.
- Chen, H., Zhou, H., Rao, Y., 2020. An implicit stabilization strategy for Q-compensated reverse time migration. Geophysics 85 (5), WB97—WB107. https://doi.org/10.1190/geo2019-0235.1
- Da Silva, N.V., Yao, G., Warner, M., 2019. Wave modeling in viscoacoustic media with transverse isotropy. Geophysics 84 (3), C41–C56. https://doi.org/10.1190/ geo2017-0695.1.
- Deng, F., McMechan, G.A., 2007. True-amplitude prestack depth migration. Geophysics 72 (3), S155–S166. https://doi.org/10.1190/1.2714334.
- Duveneck, E., Bakker, P.M., 2011. Stable P-wave modeling for reverse-time migration in tilted TI media. Geophysics 76 (2), S65–S75. https://doi.org/10.1190/
- Fathalian, A., Trad, D.O., Innanen, K.A., 2021. Q-compensated reverse time migration in tilted transversely isotropic media. Geophysics 86 (1), S73—S89. https:// doi.org/10.1190/geo2019-0466.1.
- Guo, P., McMechan, G.A., Guan, H., 2016. Comparison of two viscoacoustic propagators for Q-compensated reverse time migration. Geophysics 81 (5), S281–S297. https://doi.org/10.1190/geo2015-0557.1.
- Kjartansson, E., 1979. Constant-Q wave propagation and attenuation. J. Geophys. Res. 84 (B9), 4737–4748. https://doi.org/10.1029/JB084iB09p04737.
- Li, Z., Qu, Y., 2022. Research progress on seismic imaging technology. Pet. Sci. 19 (1), 128–146. https://doi.org/10.1016/j.petsci.2022.01.015.
- Liu, H.P., Anderson, D.L., Kanamori, H., 1976. Velocity dispersion due to anelasticity; implications for seismology and mantle composition. Geophys. J. Int. 47 (1), 41–58. https://doi.org/10.1111/j.1365-246X.1976.tb01261.x.
- Lynn, H.B., Campagna, D., Simon, K.M., et al., 1999. Relationship of P-wave seismic attributes, azimuthal anisotropy, & commercial gas pay in 3-D P-wave multiazimuth data, Rulison field, Piceance basin, Colorado. Geophysics 64 (4), 1293–1311. https://doi.org/10.1190/1.1444635.
- Mao, Q., Huang, J., Mu, X., et al., 2024a. Accurate simulations of pure-viscoacoustic wave propagation in tilted transversely isotropic media. Pet. Sci. 21 (2), 866–884. https://doi.org/10.1016/j.petsci.2023.11.005.
  Mao, Q., Huang, J., Mu, X., et al., 2024b. Efficient least-squares reverse time
- Mao, Q., Huang, J., Mu, X., et al., 2024b. Efficient least-squares reverse time migration in TTI media using a finite-difference solvable pure qP-wave equation. J. Geophys. Eng. 21 (2), 465–482. https://doi.org/10.1190/geo2023-0631.1.
- Mu, X., Huang, J., Li, Z., et al., 2022a. Attenuation compensation and anisotropy correction in reverse time migration for attenuating tilted transversely isotropic media. Surv. Geophys. 43 (3), 737–773. https://doi.org/10.1007/s10712-022-09717-0.
- Mu, X., Huang, J.P., Yang, J.D., et al., 2022b. Modelling of pure visco-qP-wave

- propagation in attenuating tilted transversely isotropic (TTI) media based on decoupled fractional Laplacians. Geophysics 87 (4), 291–313. https://doi.org/10.1190/geo2021-0440.1.
- Mu, X.R., Mao, Q., Huang, J., 2023. Stable attenuation-compensated reverse time migration and its application to land seismic data. Pet. Sci. 20 (6), 2784–2795. https://doi.org/10.1016/j.petsci.2023.03.014.
- Qu, Y., Huang, J., Li, Z., et al., 2017. Attenuation compensation in anisotropic least-squares reverse time migration. Geophysics 82 (6), S411–S423. https://doi.org/10.1190/geo2016-0677.1.
- Qu, Y., Zhu, J., Chen, Z., et al., 2022. Q-compensated least-squares reverse time migration with velocity-anisotropy correction based on the first-order velocitypressure equations. Geophysics 87 (6), S335–S350. https://doi.org/10.1190/ geo2021.06891
- Sun, R., You, J.C., Liu, N.C., 2024. Time-fractional viscoacoustic wave equation based frequency domain stable Q-RTM. IEEE Trans. Geosci. Rem. Sens. https://doi.org/ 10.1109/TGRS.2024.3444467.
- Tao, G., King, M.S., 1990. Shear-wave velocity and Q anisotropy in rocks: a laboratory study. Int. J. Rock Mech. Min. Sci. Geomech. Abstracts 27 (5), 353–361. https:// doi.org/10.1016/0148-9062(90)92710-V. Pergamon, Oxford.
- Thomsen, L., 1986. Weak elastic anisotropy. Geophysics 51 (10), 1954–1966. https://doi.org/10.1190/1.1442051.
- Wang, N., Xing, G.C., Zhu, T.Y., et al., 2022a. Propagating seismic waves in VTI attenuating media using fractional viscoelastic wave equation. J. Geophys. Res. Solid Earth 127 (4), e2021JB023280. https://doi.org/10.1029/2021JB023280.
- Wang, N., Shi, Y., Zhou, H., 2022b. Accurately stable Q-compensated reverse-time migration scheme for heterogeneous viscoelastic media. Remote Sens. 14 (19), 4782. https://doi.org/10.3390/rs14194782.
- Xiang, L., Huang, J., Mao, Q., et al., 2025. A new highly accurate and efficient pure visco-acoustic wave equation for tilted transversely isotropic attenuating media. Geophysical Prospecting 73 (3), 777–794. https://doi.org/10.1111/1365-2478.13519.
- Xie, Y., Sun, J., Zhang, Y., et al., 2015. Compensating for viscoacoustic effects in TTI reverse time migration. In: 85th Annual International Meeting, SEG, Expanded Abstracts, pp. 3996–4001. https://doi.org/10.1190/segam2015-5855445.1.
- Xing, G., Zhu, T.Y., 2019. Modeling frequency-independent Q viscoacoustic wave propagation in heterogeneous media. J. Geophys. Res. Solid Earth 124 (1), 568–584. https://doi.org/10.1029/2019JB017985.
- Xu, S., Zhou, H., 2014. Accurate simulations of pure quasi-P-waves in complex anisotropic media. Geophysics 79 (3), 341–348. https://doi.org/10.1190/ geo2014-0242.1.
- Xu, W., Li, Z., Wang, J., et al., 2015. A pure viscoacoustic equation for VTI media applied in anisotropic RTM. J. Geophys. Eng. 12 (6), 969–977. https://doi.org/ 10.1088/1742-2132/12/6/969.
- Yao, J., Zhu, T.Y., Hussain, F., et al., 2017. Locally solving fractional Laplacian viscoacoustic wave equation using Hermite distributed approximating functional method. Geophysics 82 (5), T59-T67. https://doi.org/10.1190/geo2016-0269.1.
- Yang, J.D., Huang, J.P., Zhu, H.J., et al., 2021. Viscoacoustic reverse-time migration with a robust space-wavenumber domain attenuation compensation operator. Geophysics 86 (5), S339—S353. https://doi.org/10.1190/geo2020-0608.1.
- Zhang, P., Yao, G., Zheng, Q., et al., 2024. An improved pure quasi-P-wave equation for complex anisotropic media. J. Geophys. Eng. 21 (2), 517–533. https://doi.org/10.1093/jge/gxae020.
- Zhang, Y.B., Liu, Y., Xu, S.G., 2020. Anisotropic viscoacoustic wave modelling in VTI media using frequency-dependent complex velocity. J. Geophys. Eng. 17 (5), 700–717. https://doi.org/10.1093/jge/gxaa023.
- Zhang, Y., Chen, T., Liu, Y., et al., 2022. Viscoelastic wave propagation in transversely isotropic media based on constant-order fractional polynomial approximations. Geophysics 87 (5), T363—T379. https://doi.org/10.1190/geo2021-0837.1.
- Zhou, H.Y., Liu, Y., Wang, J., 2023. Two exact first-order k-space formulations for low-rank viscoacoustic wave propagation on staggered grids. Pet. Sci. 20 (3), 1521–1531. https://doi.org/10.1016/j.petsci.2022.10.012.
- Zhu, T.Y., Harris, J.M., Biondi, B., 2014. Q-compensated reverse time migration. Geophysics 79 (4), S77–S87. https://doi.org/10.1190/geo2013-0344.1.
- Zhu, Y., Tsvankin, I., 2006. Plane-wave propagation in attenuative transversely isotropic media. Geophysics 71 (2), T17–T30. https://doi.org/10.1190/1.2187792.
- Zhu, T.Y., Bai, T., 2019. Efficient modeling of wave propagation in a vertical transversely isotropic attenuative medium based on fractional Laplacian. Geophysics 84 (3), T121–T131. https://doi.org/10.1190/geo2018-0538.1.
- Zhubayev, A., Houben, M.E., Smeulders, D.M.J., et al., 2016. Ultrasonic velocity and attenuation anisotropy of shales, Whitby, United Kingdom. Geophysics 81 (1), D45–D56. https://doi.org/10.1190/geo2015-0211.1.